Physics of Plasmas ARTICLE pubs.aip.org/aip/pop

Nonlinear mode coupling between waves in a nonneutral plasma

Cite as: Phys. Plasmas **33**, 012102 (2026); doi: 10.1063/5.0301597
Submitted: 9 September 2025 · Accepted: 10 December 2025 · Published Online: 5 January 2026

Daniel H. E. Dubin,[a] A. Kabantsev, and C. F. Driscoll

AFFILIATIONS

Department of Physics UCSD, La Jolla, California 92093, USA

[a]Author to whom correspondence should be addressed: ddubin@ucsd.edu

ABSTRACT

Nonlinear mode coupling is observed to create striking patterns of frequency splitting in waves excited on a nonneutral plasma column. The patterns are caused by the nonlinear interaction of a diocotron mode with up to five other magnetized plasma modes. The explanation of these patterns has led to the development of a novel and general eigenmode analysis for ideal fluid and plasma systems, involving inner products based on the wave energy or wave angular momentum, and with respect to which the modes form an orthogonal basis. The theory employs and clarifies the connection between conservation laws and the Hermitian (or anti-Hermitian) properties of the linearized dynamics. Consequently, the general approach to nonlinear mode coupling presented here is applicable to any ideal nonlinear inhomogeneous fluid or plasma system.

I. INTRODUCTION

Nonlinear mode coupling is a fundamental energy transfer process in systems that exhibit wavelike phenomena.[1,2] In this paper, we investigate effects caused by nonlinear mode coupling of waves on a nonneutral plasma column: mixing and frequency shifts (avoided crossings) of near-resonant magnetized plasma eigenmodes coupled through their interaction with a low-frequency diocotron wave. Nonneutral plasmas have several advantages for such studies: the plasmas can be confined for long periods of time, initial conditions are reproducible with errors of 1% or less, and the plasma waves that can be excited have a dense frequency spectrum that exhibits many possible resonances for low-order mode-coupling processes.

In Sec. II, we describe experiments in which complex frequency patterns appear during the excitation of plasma waves on a nonneutral plasma column. We explain these patterns in Secs. III–VI. In Sec. III, we briefly review the properties of the linear eigenmodes of a nonneutral plasma in the ideal cold fluid drift approximation. In Sec. IV, we derive expressions for the wave energy and angular momentum from the linearized Lagrangian for the wave system. We use these expressions to derive inner products that allow the use of the plasma eigenmodes as part of a complete orthogonal basis. This allows an elegant and complete formulation of the nonlinear mode-coupling equations for the system in Sec. V. In Sec. VI, we return to the experiments and use the mode-coupling theory to explain the experimental results in detail. The results are summarized in Sec. VII.

II. EXPERIMENTS INVOLVING SIMULTANEOUS EXCITATION OF A MAGNETIZED PLASMA WAVE AND A DIOCOTRON WAVE

An electron plasma column with a length L of roughly 34 cm is held in a cylindrical Penning–Malmberg trap, shown schematically in Fig. 1. The operating principles of such traps are described in Ref. 3. The plasma is confined axially by applying negative voltages to cylinders L2 and G10, and is confined radially by the applied uniform axial magnetic field. The plasma radius is roughly 1 cm, and the maximum electron density is roughly $1.8 \times 10^7\ \mathrm{cm}^{-3}$. The applied magnetic field in the trap is 1.3 T, and the inner radius of the surrounding electrode structure is $r_w = 3.5$ cm.

A magnetized plasma mode [Trivelpiece–Gould (TG) wave[4]] is then excited by applying five cycles of voltage oscillations to cylindrically symmetric electrode H3, at a frequency $\Omega/2\pi = 930$ kHz, chosen to be near the frequency of one of the cylindrically symmetric TG modes. (These modes are described in more detail in Secs. III and VI.) The mode decays in a few milliseconds and is then re-excited with another 5-cycle burst, once every 2 s for up to forty separate TG mode excitations. The measured decay rate of this mode, roughly

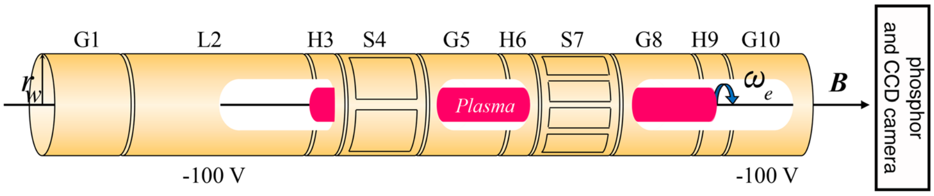

FIG. 1. Cutaway schematic of the Penning trap used in the experiments, to scale, with different electrodes labeled.

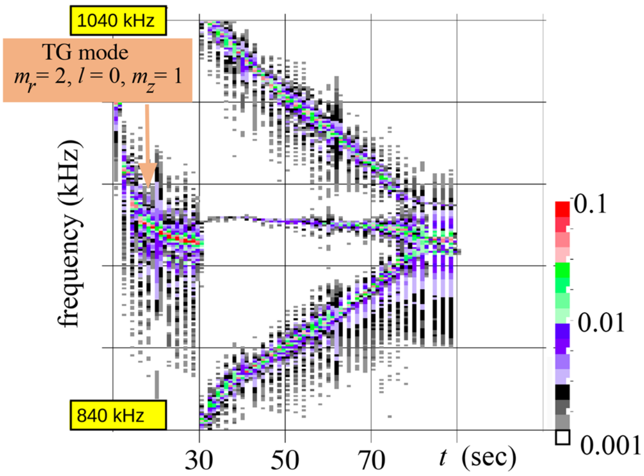

FIG. 2. Frequency spectrum vs time of plasma modes observed by monitoring a cylindrically symmetric electrode. Colors correspond to amplitude in arbitrary units on the displayed logarithmic scale. At $t = 30$ s after plasma creation, a diocotron mode with $l = 2$ is launched (Fig. 3), producing a pattern of 3 frequency peaks whose frequencies converge over time. Adapted from Ref. 8.

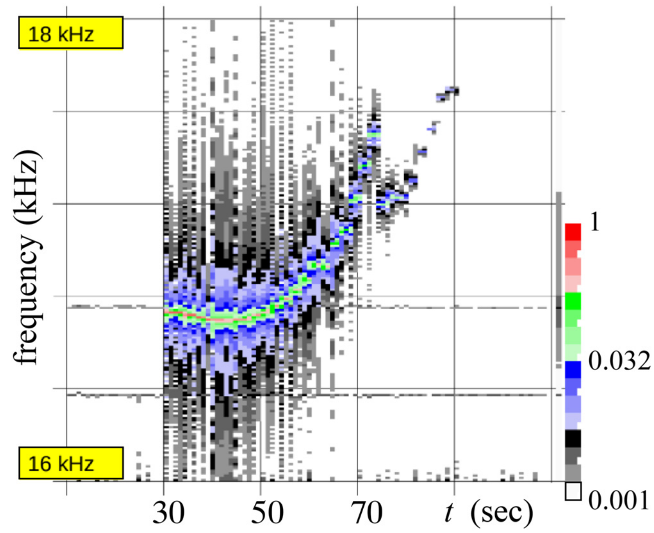

FIG. 3. Frequency spectrum for the diocotron mode, observed by monitoring a sectored electrode. Colors correspond to amplitude in arbitrary units on the displayed logarithmic scale. Adapted from Ref. 8.

$850 - 900\,\mathrm{s}^{-1}$, is due to several nonideal effects, but is mainly from finite resistance in the conducting walls and external circuits.

The plasma response to these excitations is monitored by measuring the image current induced on a second cylindrically symmetric electrode, G8. The resulting signal is digitized at a rate of 10 MHz. A spectrogram of the observed signal vs time is shown in Fig. 2. This spectrogram shows the amplitude of the fast Fourier transform of the first 2 ms of the digitized signal after each excitation, plotted at the time of each excitation. In this and in later spectrograms, the time $t = 0$ is the time at which the plasma is trapped. For the first few seconds after the plasma is trapped, the mode frequency ω_0 decreases due to cyclotron cooling of the electron temperature at a rate ν_c given by the well-known Larmor formula,[5] $\nu_c = 0.26\,\mathrm{s}^{-1}(B/1\,\mathrm{T})^2$, until an equilibrium of roughly room temperature is approached.

At time $t = 30$ s, after plasma injection and trapping, a diocotron mode[6] of relatively low frequency $\omega_D/2\pi \approx 17$ kHz is separately excited by applying oscillatory voltages to several sectors in electrode S7 (see Fig. 3). This diocotron mode has an azimuthal mode number $l = 2$, varying in θ and t as $\cos(2\theta - \omega_D t)$. Directly after the excitation of the diocotron mode, 3 new mode frequencies are detected in the image currents on the cylindrically symmetric electrode G8—one at roughly 100 kHz higher frequency than previously, one at 100 kHz lower frequency, and one at close to the original frequency. As the diocotron mode decays in amplitude over time, the frequency difference between these new wall signals decreases. (The diocotron mode frequency also increases slightly as its amplitude decays, as expected for these modes.[7]) At $t = 90$ s. the plasma is dumped onto a phosphor screen by grounding cylinder G10, in order to determine the radial electron density profile.

In Secs. III–VI, we will develop a mode-coupling theory to show that the observed frequency pattern in Fig. 2 can be explained as a 4-wave interaction between the diocotron mode and 3 nearly degenerate magnetized plasma waves. The diocotron mode acts as a pump wave that mode-couples and mixes the plasma waves. The mode-coupling theory explains both the frequency pattern and the strength of the signal for each observed frequency peak. We will also see that the theory explains other experiments that produce different frequency patterns when other TG plasma waves are excited in the presence of a diocotron wave.

III. DRIFT THEORY OF WAVES IN A NONNEUTRAL PLASMA

In this section, we briefly review the theory of electrostatic waves in a nonneutral plasma consisting of identical positive charges e of mass m, confined in a Penning trap by a time-independent externally applied potential with cylindrical symmetry, and by a uniform magnetic field in the axial $(-z)$ direction, $\boldsymbol{B} = -B\hat{z}, B > 0$.

For a nonneutral plasma consisting of identical negative charges, one should replace e by $-e$ and B by $-B$ in all equations (i.e., the magnetic field is now in the $+z$ direction). No other changes to the equations or results need to be made. For example, the $E \times B$ rotation frequency of the plasma remains in the $+\hat{\theta}$ direction, and diocotron waves continue to propagate in the $+\hat{\theta}$ direction.

For our purpose, it is sufficient to employ ideal cold fluid equations[9] in the description of these waves, involving coupled differential equations for the plasma number density $n(\boldsymbol{r}, t)$, the fluid velocity $\boldsymbol{v}(\boldsymbol{r}, t)$, and the electrostatic plasma potential $\phi(\boldsymbol{r}, t)$. This ideal cold fluid description is useful provided that the plasma temperature T is small enough that the plasma Debye length $\sqrt{T/(4\pi e^2 n)}$ is small compared to the wavelength of the waves of interest, and that nonideal effects (such as collisional, resistive, or viscous wave damping) can be ignored.

In addition, the applied magnetic field strength B is sufficiently large so that the drift approximation[10] is useful for waves with frequencies at or below the plasma frequency $\omega_p = \sqrt{4\pi e^2 n/m}$, which are the waves of interest in this paper. This approximation requires that the cyclotron frequency $\Omega_c = eB/(mc)$ be much larger than ω_p. Higher frequency electrostatic waves (such as upper hybrid waves or Bernstein waves) are not considered here, nor are electromagnetic waves.

The dynamics of the system are then described by the following fluid equations:

continuity

$$\frac{\partial n}{\partial t} + \nabla \cdot (n\boldsymbol{v}) = 0, \tag{1}$$

and parallel velocity

$$mn\left(\frac{\partial v_z}{\partial t} + \boldsymbol{v} \cdot \nabla v_z\right) = -en\frac{\partial \phi}{\partial z}, \tag{2}$$

where the total fluid velocity is $\boldsymbol{v} = \boldsymbol{v}_\perp + v_z\hat{z}$, and the perpendicular component $\boldsymbol{v}_\perp$ is given by the $E \times B$ drift velocity,

$$\boldsymbol{v}_\perp = \frac{c}{B}\nabla\phi \times \hat{z}. \tag{3}$$

This system of equations is closed by the Poisson equation,

$$\nabla^2\phi = -4\pi e n. \tag{4}$$

When the plasma is in equilibrium in applied cylindrically symmetric confinement potentials, the density is both time and θ-independent, i.e., $n = n_e(r, z)$, where $n_e(r, z)$ is the equilibrium plasma density. The corresponding total equilibrium electrostatic potential [i.e., the solution of Eq. (4)] is $\phi_e(r, z)$, and the equilibrium fluid velocity is $\boldsymbol{v}_e = r\omega_e\hat{\theta}$, where Eq. (3) implies

$$\omega_e = -\frac{c}{Br}\frac{\partial \phi_e}{\partial r} \tag{5}$$

is the equilibrium $E \times B$ rotation frequency of the plasma.

In equilibrium, Eq. (2) reduces to $-en_e\frac{\partial \phi_e}{\partial z} = 0$, so ϕ_e is independent of z inside the plasma (otherwise the z electric field would accelerate charges in the z direction). This implies through Eq. (4) that n_e is also independent of z inside the plasma, i.e., the equilibrium density is uniform in z inside the plasma and drops sharply to zero at the plasma ends, whose locations in z as a function of r are determined by the confinement voltages. This also implies, through Eq. (5), that within the plasma $\omega_e = \omega_e(r)$, i.e., the equilibrium plasma rotation frequency is independent of z.

In the experiments discussed in this paper, the equilibrium density and rotation frequency $n_e(r, z)$ and $\omega_e(r)$ are monotonically decreasing functions of r. Note that since $\omega_e(r)$ is not uniform in these experiments, this equilibrium is not a thermal equilibrium. On a timescale long compared to the timescales of interest here,[11] this equilibrium can slowly evolve toward a rigidly rotating thermal equilibrium in which ω_e is uniform in r. Slow evolution of the equilibrium can also occur due to various nonideal effects such as collisions with background gas or plasma interaction with intrinsic field errors.[12] These effects are not important in the experiments discussed here.

We now consider small perturbations from equilibrium, of the form $n(\boldsymbol{r}, t) = n_e(r, z) + \delta n(\boldsymbol{r}, t)$, $\boldsymbol{v}(\boldsymbol{r}, t) = \omega_e(r)r\hat{\theta} + \delta\boldsymbol{v}(\boldsymbol{r}, t)$, $\phi(\boldsymbol{r}, t) = \phi_e(r, z) + \delta\phi(\boldsymbol{r}, t)$. Then, to linear order in the perturbed quantities, Eqs. (1)–(4) can be reduced to

$$\frac{\partial \delta n}{\partial t} + \omega_e\frac{\partial \delta n}{\partial \theta} + \frac{c}{Br}\frac{\partial \delta\phi}{\partial \theta}\frac{\partial n_e}{\partial r} + \frac{\partial}{\partial z}(n_e\delta v_z) = 0, \tag{6}$$

$$\frac{\partial \delta v_z}{\partial t} + \omega_e\frac{\partial \delta v_z}{\partial \theta} = -\frac{e}{m}\frac{\partial \delta\phi}{\partial z}, \tag{7}$$

$$\nabla^2\delta\phi = -4\pi e\delta n. \tag{8}$$

These are the linear equations of motion for perturbations to the plasma.

A. The state vector and eigenmode expansions of the linear dynamics

It is useful to introduce the state vector $\boldsymbol{\chi}(\boldsymbol{r}, t) = (\delta n, \delta v_z)$ that describes the state of perturbations to the cold fluid system at time t. In vector form, Eqs. (6)–(8) can then be expressed as

$$\frac{\partial \boldsymbol{\chi}}{\partial t} + \hat{\boldsymbol{L}} \cdot \boldsymbol{\chi} = 0, \tag{9}$$

where the linear integrodifferential operator $\hat{\boldsymbol{L}}$ is

$$\hat{\boldsymbol{L}} \cdot \boldsymbol{\chi} = \begin{pmatrix} \omega_e\frac{\partial}{\partial \theta}\delta n + \frac{c}{Br}\frac{\partial n_e}{\partial r}\frac{\partial}{\partial \theta}\hat{G}\delta n + \frac{\partial}{\partial z}(n_e\delta v_z) \\ \omega_e\frac{\partial}{\partial \theta}\delta v_z + \frac{e}{m}\frac{\partial}{\partial z}\hat{G}\delta n \end{pmatrix}, \tag{10}$$

where $\hat{G}$ is the Green's function operator for the Poisson equation, defined by $\delta\phi = \hat{G}\delta n$.

Equation (9) admits solutions that oscillate in time with frequency ω, $\boldsymbol{\chi}(\boldsymbol{r}, t) = \boldsymbol{\psi}(\boldsymbol{r})e^{-i\omega t}$, which implies

$$\hat{\boldsymbol{L}} \cdot \boldsymbol{\psi} = i\omega\boldsymbol{\psi}. \tag{11}$$

These oscillatory solutions are the eigenmodes of the linear dynamics. The eigenmodes fall into two categories: "dynamical" eigenmodes with $\omega \neq 0$, and "equilibrium" eigenmodes with $\omega = 0$. The dynamical modes are the standard plasma wave solutions for the bounded plasma. The equilibrium modes are perturbations that take the system from one equilibrium to another; for example, an equilibrium with a different radial density and rotation profile. The equilibrium modes are often neglected in discussions of plasma waves, but such zero-frequency modes have been used in other contexts to describe certain zonal flows[13] in plasma and fluids, geostrophic modes[14] in geophysical flows, and zero-energy modes in condensed matter systems.[15]

A general state vector $\boldsymbol{\chi}(\boldsymbol{r},t)$ can be decomposed as a linear combination of these eigenmodes,

$$\boldsymbol{\chi} = \sum_{\alpha} a_{\alpha}(t)\boldsymbol{\psi}_{\alpha}(\boldsymbol{r}), \tag{12}$$

where α is a counter (or a set of counters) enumerating the different eigenmodes.

Note that, since the state vector $\boldsymbol{\chi}$ is, generally speaking, taken to be a real quantity, and the eigenmodes are not necessarily real, a symmetry property is necessary in order to guarantee that the sum over the modes in Eq. (12) yields a real result: for every eigenfunction $\boldsymbol{\psi}_{\alpha}$ with frequency $\omega_{\alpha} \neq 0$, there is a second eigenfunction $\boldsymbol{\psi}_{\alpha}^{*}$ with frequency $-\omega_{\alpha}^{*}$. This follows by taking the complex conjugate of Eq. (9) and using the fact that $\hat{\boldsymbol{L}}$ is real-valued. The complex-conjugate modes entering Eq. (12) allow the sum to evaluate to a real quantity.

This eigenmode decomposition is facilitated by the fact, proven in Sec. IV, that the eigenmodes form an orthogonal set with respect to either of two inner products that are based on integral constants of the motion: the total energy and the canonical angular momentum. The energy E_{α} of a given dynamical eigenmode labeled α is given in terms of the energy-based inner product by $E_{\alpha} = \langle\boldsymbol{\psi}_{\alpha},\boldsymbol{\psi}_{\alpha}\rangle_E$, and angular momentum $P_{\theta\alpha}$ of the dynamical mode is given by a second inner product, $P_{\theta\alpha} = \langle\boldsymbol{\psi}_{\alpha},\boldsymbol{\psi}_{\alpha}\rangle_{P_\theta}$. We will derive expressions for the inner products in Sec. IV.

These inner products are generalized inner products, in the sense that $\langle\boldsymbol{\psi}_{\alpha},\boldsymbol{\psi}_{\alpha}\rangle_E$ and $\langle\boldsymbol{\psi}_{\alpha},\boldsymbol{\psi}_{\alpha}\rangle_{P_\theta}$ can be either negative or positive, or even zero. For example, it is well-known that the z–independent perturbations associated with diocotron oscillations on a plasma column have negative energy and angular momentum.[16] Also, $P_{\theta\alpha} = 0$ for θ-independent modes.

Note that, for completeness, all eigenmodes must be kept in Eq. (12), including equilibrium eigenmodes. During nonlinear evolution, the equilibrium can evolve; for example, as in the nonlinear evolution of the radial density profile during spatial Landau damping of diocotron modes,[17] or in the zonal flows induced by Reynolds stress in turbulent fluids or plasmas.[13] Zero-frequency equilibrium eigenmodes must be included in Eq. (12) to fully capture such behavior. However, in this paper, we will consider nonlinear processes where the equilibrium evolution can be neglected, so we will not have need for the equilibrium modes.

Orthogonality of the eigenmodes with respect to the inner products, i.e., $\langle\boldsymbol{\psi}_{\alpha},\boldsymbol{\psi}_{\beta}\rangle_E = \langle\boldsymbol{\psi}_{\alpha},\boldsymbol{\psi}_{\beta}\rangle_{P_\theta} = 0$ for $\alpha \neq \beta$, implies that the Fourier coefficients a_{α} in Eq. (12) can be determined either by

$$a_{\alpha} = \frac{\langle\boldsymbol{\psi}_{\alpha},\boldsymbol{\chi}\rangle_E}{E_{\alpha}}, \tag{13}$$

or by

$$a_{\alpha} = \frac{\langle\boldsymbol{\psi}_{\alpha},\boldsymbol{\chi}\rangle_{P_\theta}}{P_{\theta\alpha}}, \tag{14}$$

with the caveats that $E_{\alpha} \neq 0$ and $P_{\theta\alpha} \neq 0$. Typically, the eigenmodes have nonzero energy and/or angular momentum in a linearly stable equilibrium.

It should be noted that eigenmode expansions similar to Eqs. (12)–(14) have been employed in many previous plasma physics and fluid dynamics applications. For example, in the simplest versions, the equilibrium is assumed to be uniform in space so that the eigenmodes are standard Fourier modes, with straightforward orthogonality relations.[2] In more general systems with spatially nonuniform equilibria, special cases are scattered through the literature for which eigenmodes are found to be orthogonal with respect to some inner product. Examples include diocotron waves,[17] TG waves in the infinite magnetic field limit,[18] electromagnetic waves in a plasma-filled cylindrical waveguide,[19] and systems that can be reduced to a Sturm–Liouville problem, such as shallow water waves.[20]

However, for the general TG plasma modes discussed in this paper, no inner product has been found previously that allows the modes to be used as an orthogonal basis. Furthermore, the method we outline in this paper allows the construction of such inner products for any linear wave system with conserved quantities, such as energy or momentum, that are quadratic in the dynamical variables.

A general approach to eigenmode expansions for inhomogeneous equilibria, that uses left eigenmodes (the modes of an operator adjoint to $\hat{\boldsymbol{L}}$ for some given [but arbitrary] inner product), can also be employed to determine the Fourier coefficients a_{α}.[21] However, that method involves inner products between left and right eigenmodes, to which it can be difficult to attach physical significance. In our approach, the inner products are related to constants of the motion, and only the physically relevant right eigenmodes of the dynamical system are required, allowing a clear physical interpretation of the theory.

B. Dynamical eigenmodes of a long plasma column

A standard theory approximation for the dynamical eigenmodes of a long plasma column is to assume flat, stationary plasma ends at $z = 0$ and $z = L$, neglecting the effect of the confining end potentials on the modes, which allows a simplified description of eigenmode z-dependence.[24] This approximation works best for cylindrical plasmas that are long compared to their radius,[26,27] which is the case in the experiments of interest here. Even so, the approximation can sometimes break down due to linear mode coupling caused by the confinement potentials when certain resonance conditions are met.[18] We ignore this possibility here. Eigenmode density, potential, and axial velocity then take the simplified form

$$\begin{aligned} \delta n_{\alpha}(\boldsymbol{r},t) &= N_{\alpha}(r)e^{il\theta - i\omega_{\alpha}t}\cos(k_z z),\\ \delta\phi_{\alpha}(\boldsymbol{r},t) &= \Phi_{\alpha}(r)e^{il\theta - i\omega_{\alpha}t}\cos(k_z z),\\ \delta v_{z\alpha}(\boldsymbol{r},t) &= iV_{\alpha}(r)e^{il\theta - i\omega_{\alpha}t}\sin(k_z z), \end{aligned} \tag{15}$$

where the axial wavenumber $k_z = m_z\pi/L$ is quantized by the axial mode number m_z, a nonnegative integer. These modes are standing waves in z and r, and traveling waves in θ. The functions $N_{\alpha}(r), \Phi_{\alpha}(r)$, and $V_{\alpha}(r)$ are real-valued. Equations (6) and (7) relate them to one another

$$N_{\alpha}(r) = \left(\frac{lc}{Br\hat{\omega}_{\alpha}}\frac{\partial n_e}{\partial r} + \frac{ek_z^2}{m\hat{\omega}_{\alpha}^2}n_e\right)\Phi_{\alpha}(r), \tag{16}$$

$$V_{\alpha}(r) = \frac{ek_z}{m\hat{\omega}_{\alpha}}\Phi_{\alpha}(r), \tag{17}$$

where $\hat{\omega}_{\alpha}(r) \equiv \omega_{\alpha} - l\omega_e(r)$ is the Doppler-shifted mode frequency. [Equations (16) and (17) assume that $\hat{\omega}_{\alpha} \neq 0$, so they do not hold for the continuum modes discussed below.] These modes have been discussed in detail in several previous publications (see, for example, Refs. 4, 24, 25, and 27) so we will only briefly summarize some of their relevant properties here.

There are two types of dynamical eigenmodes: "discrete" modes and "continuum" modes. The continuum modes have singular density and potential eigenfunctions due to a resonance at a radius within the plasma, where $\omega_\alpha = l\omega_e(r)$.[17,28] For every radius r within the plasma, there is a frequency ω_α that satisfies this resonance condition, so the spectrum for these modes is continuous.

On the other hand, the discrete eigenmodes have a discrete frequency spectrum, and smooth density and potential eigenfunctions. These discrete modes can be further classified as either a $k_z = 0$ diocotron "surface mode" or $k_z \neq 0$ "magnetized plasma" modes.

For the discrete magnetized plasma and diocotron modes, Eqs.(6)–(8) can be combined, using Eqs. (15)–(17), into a single ordinary differential equation for the radial dependence of the mode potential $\Phi_\alpha(r)$,

$$\frac{1}{r}\frac{\partial}{\partial r}\left(r\frac{\partial \Phi_\alpha}{\partial r}\right) - \left(\frac{l^2}{r^2}+k_z^2\right)\Phi_\alpha + \frac{\omega_p^2(r)}{\hat{\omega}_\alpha^2}k_z^2\Phi_\alpha + \frac{4\pi ecl}{Br\hat{\omega}_\alpha}\frac{\partial n_e}{\partial r}\Phi_\alpha = 0, \quad (18)$$

with boundary conditions that $\Phi_\alpha(r_w) = 0$ and $\Phi_\alpha(r = 0)$ is noninfinite, and where $\omega_p(r) = \sqrt{4\pi e^2 n_e(r)/m}$ is the plasma frequency. (Similar differential equations can be derived for the continuum modes.[7]) Since the equation and boundary conditions are homogeneous, this is an eigenvalue problem for ω_α. For general equilibrium radial density profiles, the problem can be solved numerically to provide $\Phi_\alpha(r)$ and ω_α, for example, via the shooting method; analytic solutions can be obtained in some special cases.[4,29]

A diocotron mode with positive azimuthal phase velocity occurs at $k_z = 0$ for each $l \neq 0$, up to some maximum value of $|l|$ which depends on the equilibrium density profile. For $|l|$ greater than this maximum value, the diocotron mode is absorbed into the continuum modes, causing spatial Landau damping of the mode.[17] The diocotron modes are surface density waves on the plasma column, traveling in θ only in the $+\theta$ direction (i.e., the direction of plasma rotation). The potentials for these diocotron modes are shown in Fig. 4. For the experimentally measured density profile shown in Fig. 5, only $|l| = 1$ and 2 diocotron modes are discrete.

The magnetized plasma modes, with $k_z \neq 0$, are compressional plasma waves. For given values of l and k_z there is a set of magnetized

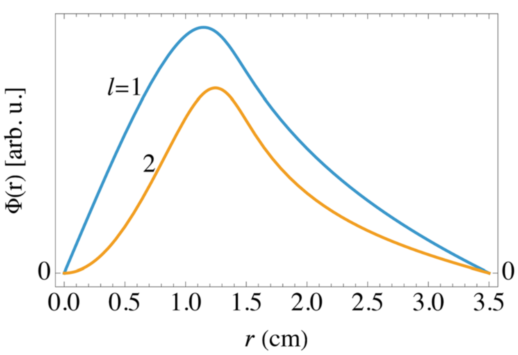

FIG. 4. Radial dependence of the diocotron mode potential $\Phi_D(r)$, in arbitrary units, for $l = 1$ and 2, for the density profile shown in Fig. 5.

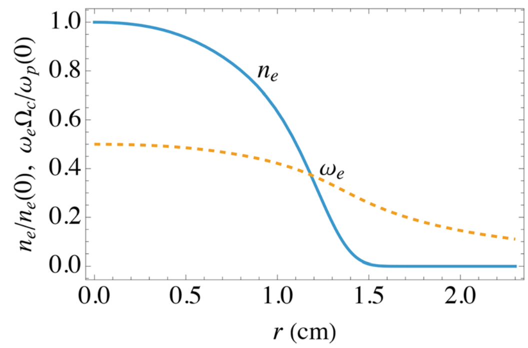

FIG. 5. Experimentally measured equilibrium density n_e and corresponding rotation frequency ω_e used for the eigenmodes shown in Figs. 4 and 6. The measured central density is $n_e(r = 0) = 1.81 \times 10^7\ \mathrm{cm}^{-3}$.

plasma modes, each with a different degree of oscillation as a function of radius. These modes may be enumerated using an integer index m_r (the radial mode number) increasing from $m_r = 1$, the value that corresponds to the lowest-order radial mode with no zeroes in the potential $\Phi_\alpha(r)$ within the plasma (excluding the origin); and $m_r > 1$ corresponding to $m_r - 1$ potential zeroes; see Fig. 6 for examples. Larger m_r or $|l|$ produces lower-mode frequencies; larger k_z produces higher frequencies.

For $\omega_\alpha/l > 0$, the magnetized plasma modes travel around the plasma column with positive azimuthal phase velocities, i.e., they travel in the same direction as the plasma rotation. Magnetized plasma modes with $\omega_\alpha/l < 0$ travel against the rotational plasma flow. Such modes are thus, respectively, analogous to the fast and slow electrostatic waves in a beam plasma.[30]

The oscillations of the perturbed potential as a function of radius for the magnetized plasma modes shown in Fig. 6 are reminiscent of the behavior of Bessel functions. In fact, for a uniform plasma column of radius r_p, with uniform rotation frequency, the eigenfunctions can be described analytically in terms of Bessel functions:[4]

$$\Phi_\alpha(r) = J_l(k_\perp r), \quad r < r_p, \quad (19)$$

where $J_l(x)$ is a Bessel function of the first kind, and $k_\perp$, the "perpendicular wavenumber", is given by solutions to the equation:

$$k_\perp r_p J_l'(k_\perp r_p) + \frac{2l\omega_e}{\omega_\alpha - l\omega_e}J_l(k_\perp r_p) = J_l(k_\perp r_p)k_z r_p \frac{I_l'(k_z r_p)K_l(k_z r_w) - I_l(k_z r_w)K_l'(k_z r_p)}{I_l(k_z r_p)K_l(k_z r_w) - I_l(k_z r_w)K_l(k_z r_p)}, \quad (20)$$

with mode frequency ω_α given by

$$\omega_\alpha - l\omega_e = \pm\frac{k_z\omega_p}{\sqrt{k_z^2 + k_\perp^2}}, \quad (21)$$

and where $I_l(x)$ and $K_l(x)$ are the modified Bessel functions of the first and second kinds, respectively,[31] and primes denote derivatives with respect to the argument.

For given values of k_z and l the solutions of Eq. (20) for $k_\perp$ are enumerated by the mode number m_r with increasing $k_\perp$ for increasing m_r. These solutions must be found numerically in general, but the $k_\perp$ values can also be related in certain cases to the zeros of

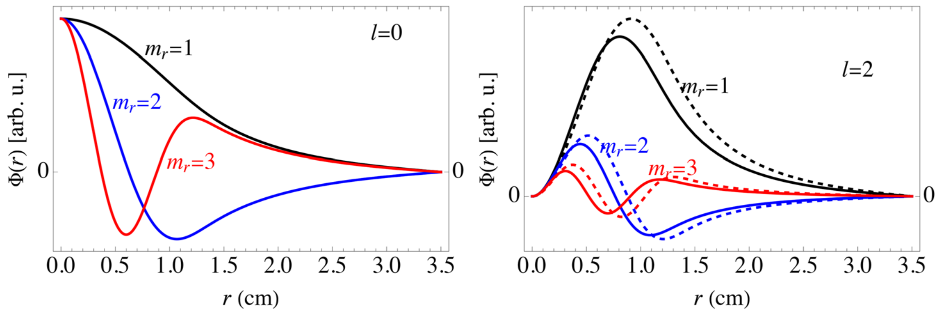

FIG. 6. Radial dependence of the magnetized plasma mode potential $\Phi_\alpha(r)$, in arbitrary units, for 3 values of radial mode number m_r, and for two values of azimuthal mode number l, for the equilibrium density profile shown in Fig. 5, assuming that $k_z = 1\,\mathrm{cm}^{-1}$, and $\Omega_c/\omega_p(r=0) = 10$. For $l = 2$, the dashed curves correspond to modes with $\omega_\alpha/l < 0$, and solid curves correspond to $\omega_\alpha/l > 0$.

Bessel functions.[24] In Sec. VI we will see that this Bessel behavior is responsible for frequency degeneracies between different modes that can lead to strong nonlinear coupling between the modes.

IV. CONSTANTS OF THE MOTION, INNER PRODUCTS, ORTHOGONALITY, AND OTHER RELATIONS

In this section, we derive constants of the motion for the linear wave dynamics. We then derive inner products based on these constants of the motion, and prove orthogonality relations involving these inner products, which facilitate a description of the system as a superposition of the system eigenmodes.

Constants of the motion can be derived in a number of ways. One of the most elegant methods is through the use of a Lagrangian framework, described below.

A. Lagrangian description and constants of the motion

The linearized electrostatic cold fluid drift equations (or any ideal fluid equations) have a Lagrangian formulation[32,33] that can be employed to derive expressions for certain integral constants of the motion, i.e., the energy and the canonical angular momentum. For Eqs. (6)–(8), the fluid Lagrangian L is a quadratic functional of Lagrangian fluid variables $\boldsymbol{\eta} \equiv (\delta\boldsymbol{r}(\boldsymbol{r},t), \delta\phi(\boldsymbol{r},t))$ where $\delta\boldsymbol{r}(\boldsymbol{r},t) = \delta r\hat{r} + r\delta\theta\hat{\theta} + \delta z\hat{z}$ is the perturbed position of a fluid element at time t. The Lagrangian is

$$L = \int d^3r\mathscr{L}, \tag{22}$$

where the Lagrangian density $\mathscr{L}$ is

$$\mathscr{L} = n_e(r,z)\left[\frac{1}{2}m(\hat{D}\delta z)^2 - e\delta\boldsymbol{r}\cdot\nabla\delta\phi + \frac{eB}{2c}r\frac{\partial\omega_e}{\partial r}\delta r^2 - \frac{eB}{c}r\delta r\hat{D}\delta\theta\right] + |\nabla\delta\phi|^2/8\pi, \tag{23}$$

and where

$$\hat{D} \equiv \frac{\partial}{\partial t} + \omega_e(r)\frac{\partial}{\partial\theta} \tag{24}$$

is the total time derivative along an unperturbed trajectory. This Lagrangian density can be derived, using the method described in Ref. 34, from the general nonlinear electrostatic Lagrangian density $\mathscr{L}^{\mathrm{NL}}$ for drift dynamics in a uniform magnetic field,

$$\mathscr{L}^{\mathrm{NL}} = n_i(\boldsymbol{r}_i)\left[\frac{1}{2}m\left(\frac{dz}{dt}(\boldsymbol{r}_i,t)\right)^2 - e\phi(\boldsymbol{r}(\boldsymbol{r}_i,t),t) - \frac{eB}{2c}r(\boldsymbol{r}_i,t)^2\frac{d\theta}{dt}(\boldsymbol{r}_i,t)\right] + |\nabla\phi|^2/(8\pi),$$

where $\boldsymbol{r}_i$ is an initial position of a fluid element and $n_i(\boldsymbol{r})$ is the initial density.

The action principle

$$\delta\int Ldt = 0 \tag{25}$$

then leads directly to the following Euler–Lagrange equations for the perturbed motion of a fluid element,

$$\hat{D}\delta r = \frac{c}{Br}\frac{\partial\delta\phi}{\partial\theta}, \tag{26}$$

$$\hat{D}\delta\theta = \frac{\partial\omega_e}{\partial r}\delta r - \frac{c}{Br}\frac{\partial\delta\phi}{\partial r}, \tag{27}$$

$$m\hat{D}^2\delta z = -e\frac{\partial\delta\phi}{\partial z}, \tag{28}$$

$$\nabla^2\delta\phi = 4\pi e\nabla\cdot(n_e\delta\boldsymbol{r}). \tag{29}$$

These equations of motion are fully consistent with the previous linearized equations of motion, Eqs. (6)–(8). This is shown in detail in Appendix B. There we also show that the Lagrangian variables $\delta r, \delta\theta$, and δz are completely determined by the Eulerian variables δv_z and δn.

Thus, the state of the system as a function of time is fully specified by $\delta v_z(\boldsymbol{r},t)$ and $\delta n(\boldsymbol{r},t)$. This is to be expected since the linearized fluid Eqs. (6)–(8) can be integrated forward in time without reference to δr, $\delta\theta$, or δz.

We are now in a position to derive constants of the motion using the linearized fluid Lagrangian. Note that the Lagrangian density (23) can be written as a function of the Lagrangian variables $\boldsymbol{\eta}$ together with their first derivatives in position and time, i.e.,

$$\mathscr{L} = \mathscr{L}(\boldsymbol{\eta}, \dot{\boldsymbol{\eta}}, \nabla\boldsymbol{\eta}, r, z), \tag{30}$$

(where $\dot{}$ refers to a partial time derivative). Then, general arguments for such Lagrangians[33] imply that the energy E, a conserved quantity, is given by

$$E = \int d^3r\left[\dot{\boldsymbol{\eta}}\cdot\frac{\partial\mathscr{L}}{\partial\dot{\boldsymbol{\eta}}} - \mathscr{L}\right]. \tag{31}$$

As shown in Appendix B, this expression can be manipulated into the following form for the wave energy:

$$E=\int d^3r\left[\frac{1}{2}mn_e\delta v_z^2+\frac{1}{2}e\delta n\delta\phi-\omega_e\frac{eB}{c}r\delta r\left(\delta n+\frac{1}{2}\delta r\frac{\partial n_e}{\partial r}\right)\right]. \quad (32)$$

The first and second terms in the energy are clearly kinetic energy and potential energy contributions, respectively. The third term, however, may not be as familiar. Given that it is proportional to the equilibrium rotation rate $\omega_e(r)$, we might then identify $-\frac{eB}{c}r\delta r\left(\delta n+\frac{1}{2}\delta r\frac{\partial n_e}{\partial r}\right)$ as an angular momentum density $p_\theta(\boldsymbol{r},t)$ so that, when ω_e is uniform, the last term has the expected form[23] for a rigidly rotating body, $\omega_e P_\theta$ where $P_\theta=\int d^3r p_\theta$ is the total angular momentum of the body. In fact, we will now see that this is the case.

Total angular momentum P_θ is also a constant of the motion due to the cylindrical symmetry of the external applied potentials, manifested in the fact that $\mathscr{L}(\boldsymbol{\eta},\dot{\boldsymbol{\eta}},\nabla\boldsymbol{\eta},r,z)$ is explicitly independent of azimuthal angle θ. The total angular momentum can then be derived from the Lagrangian density as[33]

$$P_\theta=-\int d^3r\frac{\partial\boldsymbol{\eta}}{\partial\theta}\cdot\frac{\partial\mathscr{L}}{\partial\dot{\boldsymbol{\eta}}}. \quad (33)$$

After some algebra described in Appendix B, this expression for the wave angular momentum can be reduced to

$$P_\theta=\int d^3r(-)\frac{eB}{c}r\delta r\left[\delta n+\frac{1}{2}\delta r\frac{\partial n_e}{\partial r}\right]. \quad (34)$$

The integrand is equal to the angular momentum density p_θ that appears in Eq. (32).

As a check, we can compare Eq. (34) to a previously derived expression for the angular momentum of z-independent perturbations in a long plasma column. For such perturbations, $\delta z=\delta v_z=0$. Then, Eq. (B3) implies $\delta n=-\delta r\frac{\partial n_e}{\partial r}$, and Eq. (34) becomes

$$P_\theta=\int d^3r\frac{eB}{2c}r\delta r^2\frac{\partial n_e}{\partial r}=\int d^3r\frac{eBr}{2c}\frac{\delta n^2}{\frac{\partial n_e}{\partial r}}. \quad (35)$$

This expression agrees with the wave angular momentum for z-independent perturbations derived in Ref. 7 using a different method.

B. Inner products

The integral constants of the motion E and P_θ are quadratic in the perturbed dynamical variables, and therefore can be used to define two separate inner products, each of which can be helpful in analyzing the linear or nonlinear equations of motion. We construct these inner products using the following general argument. Consider an integral constant of the motion P for the linear dynamics, with the quadratic form

$$P=\int d^3r\,\boldsymbol{\chi}\cdot\hat{\boldsymbol{P}}\cdot\boldsymbol{\chi}, \quad (36)$$

where $\boldsymbol{\chi}$ is a vector of the perturbed quantities needed to determine the state of the system, and $\hat{\boldsymbol{P}}$ is a real-valued spatial operator independent of time, acting on both left and right state vectors.

We can define a generalized inner product based on this constant of the motion in the following manner:

$$\langle\boldsymbol{\chi}_1,\boldsymbol{\chi}_2\rangle_P\equiv\int d^3r\boldsymbol{\chi}_1^*\cdot\hat{\boldsymbol{P}}^s\cdot\boldsymbol{\chi}_2, \quad (37)$$

where $\hat{\boldsymbol{P}}^s=\frac{1}{2}(\hat{\boldsymbol{P}}+\hat{\boldsymbol{P}}^t)$ is the symmetrized operator, and $\hat{\boldsymbol{P}}^t$ is the transpose of $\hat{\boldsymbol{P}}$, defined as $\int d^3r\boldsymbol{\chi}_1\cdot\hat{\boldsymbol{P}}^t\cdot\boldsymbol{\chi}_2\equiv\int d^3r\boldsymbol{\chi}_2\cdot\hat{\boldsymbol{P}}\cdot\boldsymbol{\chi}_1$. [As an aside, the symmetric form of Eq. (36) implies that one can choose to define $\hat{\boldsymbol{P}}$ such that $\hat{\boldsymbol{P}}=\hat{\boldsymbol{P}}^s$.]

It is then not difficult to show that this inner product satisfies the property $\langle\boldsymbol{\chi}_1,\boldsymbol{\chi}_2\rangle_P=\langle\boldsymbol{\chi}_2,\boldsymbol{\chi}_1\rangle_P^*$, a required property for any inner product.

For example, for our plasma system, the state vector can be taken as $\boldsymbol{\chi}=(\delta n,\delta v_z)$, as previously discussed, with other perturbed quantities $\delta\phi$ and $\delta\boldsymbol{r}$ determined in terms of $\boldsymbol{\chi}$ by relations (8), (B4), (B5), and (B8). Then, using Eq. (32), we may define an energy-based inner product between any two (possibly complex) state vectors $\boldsymbol{\chi}_1(\boldsymbol{r})=(\delta n_1,\delta v_{z1})$, $\boldsymbol{\chi}_2(\boldsymbol{r})=(\delta n_2,\delta v_{z2})$ as

$$\langle\boldsymbol{\chi}_1,\boldsymbol{\chi}_2\rangle_E\equiv\frac{1}{2}\int d^3r\left[mn_e\delta v_{z1}^*\delta v_{z2}+e\delta\phi_1^*\delta n_2\right.$$
$$\left.-\omega_e\frac{eBr}{c}\left(\delta n_1^*\delta r_2+\delta r_1^*\delta n_2+\frac{\partial n_e}{\partial r}\delta r_1^*\delta r_2\right)\right], \quad (38)$$

and Eq. (34) may be used to define a second inner product based on angular momentum,

$$\langle\boldsymbol{\chi}_1,\boldsymbol{\chi}_2\rangle_{P_\theta}\equiv-\frac{eB}{2c}\int d^3r\,r\left(\delta n_1^*\delta r_2+\delta r_1^*\delta n_2+\frac{\partial n_e}{\partial r}\delta r_1^*\delta r_2\right). \quad (39)$$

If $\boldsymbol{\chi}_1=\boldsymbol{\chi}_2=\boldsymbol{\chi}$, then $\langle\boldsymbol{\chi},\boldsymbol{\chi}\rangle_E=E$, the energy associated with the state vector $\boldsymbol{\chi}$, and $\langle\boldsymbol{\chi},\boldsymbol{\chi}\rangle_{P_\theta}=P_\theta$, the angular momentum of the state.

Some useful properties of these inner products will be derived in Subsection IV C.

C. Eigenmodes, orthogonality, and completeness

As we previously discussed, an eigenmode $\boldsymbol{\psi}$ of the linear system, with frequency ω, satisfies the eigenvalue problem Eq. (11) involving the linear operator $\hat{\boldsymbol{L}}$. Here, we consider the following general properties of these eigenmodes. We consider real-valued operators $\hat{\boldsymbol{L}}$ with a quadratic integral of the motion $P=\int d^3r\,\boldsymbol{\chi}\cdot\hat{\boldsymbol{P}}\cdot\boldsymbol{\chi}$ (which could be energy, angular momentum, or some other integral), and an associated inner product $\langle\boldsymbol{\chi}_1,\boldsymbol{\chi}_2\rangle_P$; see Eqs. (36) and (37).

(1) *Mode orthogonality*. Any two eigenmodes $\boldsymbol{\psi}_\alpha$ and $\boldsymbol{\psi}_\beta$, with frequencies ω_α and ω_β, respectively, satisfy $\langle\boldsymbol{\psi}_\alpha,\boldsymbol{\psi}_\beta\rangle_P=0$ provided that $\omega_\alpha\neq\omega_\beta^*$.
(2) *Linear stability*. If an eigenmode $\boldsymbol{\psi}_\alpha$ satisfies $\langle\boldsymbol{\psi}_\alpha,\boldsymbol{\psi}_\alpha\rangle_P\neq 0$, then the eigenfrequency ω_α is real.

These two properties follow from the well-known spectral theorem[35] for Hermitian operators. A proof of the theorem is supplied in Appendix A. To apply this theorem, we require that the operator $\hat{\boldsymbol{L}}$ be anti-Hermitian with respect to the inner product $\langle\cdot,\cdot\rangle_P$, so that $-i\hat{\boldsymbol{L}}$ is Hermitian. The following argument proves the anti-Hermitian property of $\hat{\boldsymbol{L}}$.

The fact that P is a constant of the linearized equations of motion implies, through Eqs. (36) and (9), that

$$\dot{P}=\int d^3r(\dot{\boldsymbol{\chi}}\cdot\hat{\boldsymbol{P}}\cdot\boldsymbol{\chi}+\boldsymbol{\chi}\cdot\hat{\boldsymbol{P}}\cdot\dot{\boldsymbol{\chi}})=-2\int d^3r\,\boldsymbol{\chi}\cdot\hat{\boldsymbol{P}}^s\cdot\hat{\boldsymbol{L}}\cdot\boldsymbol{\chi}=0. \quad (40)$$

Equation (40) is true for all state vectors $\boldsymbol{\chi}$, and therefore the combination operator $\hat{\boldsymbol{P}}^s\cdot\hat{\boldsymbol{L}}$ is an antisymmetric operator (the operator equivalent of an antisymmetric tensor). This implies immediately that, for any two (possibly complex) state vectors $\boldsymbol{\chi}_1$ and $\boldsymbol{\chi}_2$,

$$\int d^3r\,\boldsymbol{\chi}_1^* \cdot \hat{\boldsymbol{P}}^s \cdot \hat{\boldsymbol{L}} \cdot \boldsymbol{\chi}_2 = -\int d^3r\,\boldsymbol{\chi}_2 \cdot \hat{\boldsymbol{P}}^s \cdot \hat{\boldsymbol{L}} \cdot \boldsymbol{\chi}_1^*, \tag{41}$$

which, from Eq. (37) and the fact that $\hat{\boldsymbol{L}}$ is real-valued, is equivalent to $\langle \boldsymbol{\chi}_1, \hat{\boldsymbol{L}} \cdot \boldsymbol{\chi}_2\rangle_P = -\langle \boldsymbol{\chi}_2, \hat{\boldsymbol{L}} \cdot \boldsymbol{\chi}_1\rangle_P^*$. This proves that the operator $\hat{\boldsymbol{L}}$ is anti-Hermitian with respect to this inner product.

In addition to the above properties of the eigenmodes of the real-valued anti-Hermitian operator $\hat{\boldsymbol{L}}$, it may be shown that the eigenmodes also compose a complete set in the sense that linear superpositions of the modes exhibit convergence in the mean.[36] We may therefore expand any "sufficiently well-behaved" state vector $\boldsymbol{\chi}(\boldsymbol{r}, t)$ as a superposition of these eigenmodes.

D. Some inner product relations

Finally, we derive a few relations that simplify inner products involving the dynamical eigenmodes. We begin with an expression for the inner product $\langle \boldsymbol{\psi}_\alpha, \boldsymbol{\chi}\rangle$ of an eigenmode $\boldsymbol{\psi}_\alpha = (\delta n_\alpha, \delta v_{z,\alpha})$ and a general state vector $\boldsymbol{\chi} = (\delta n, \delta v_z)$,

$$\langle \boldsymbol{\psi}_\alpha, \boldsymbol{\chi}\rangle_E = \frac{1}{2}\int d^3r \left[m n_e \delta v_{z,\alpha}^* \delta v_z + e\delta\phi_\alpha^* \delta n - \omega_e \frac{eBr}{c}\left(\delta r_\alpha^* \delta n + \delta n_\alpha^* \delta r + \frac{\partial n_e}{\partial r}\delta r_\alpha^* \delta r\right)\right]. \tag{42}$$

Assuming this eigenmode is dynamical and discrete, some algebra detailed in Appendix B leads to the fairly simple result

$$\langle \boldsymbol{\psi}_\alpha, \boldsymbol{\chi}\rangle_E = \frac{1}{2}\int d^3r \frac{\omega_\alpha}{\hat{\omega}_\alpha}\left[m n_e \delta v_{z,\alpha}^* \delta v_z + e\delta\phi_\alpha^* \delta n\right]. \tag{43}$$

Taking $\boldsymbol{\chi} = \boldsymbol{\psi}_\alpha$, we immediately find a simplified expression for the energy E_α of a discrete dynamical eigenmode $\boldsymbol{\psi}_\alpha$,

$$E_\alpha = \frac{1}{2}\int d^3r \frac{\omega_\alpha}{\hat{\omega}_\alpha}\left[m n_e |\delta v_{z,\alpha}|^2 + e\delta\phi_\alpha^* \delta n_\alpha\right]. \tag{44}$$

A similar set of manipulations applied to Eq. (34) yields the following well-known relation[22] between angular momentum and energy for a dynamical eigenmode,

$$\omega_\alpha P_{\theta\alpha} = l E_\alpha. \tag{45}$$

We will also have occasion to consider the constants of the motion as seen in frames rotating with respect to the laboratory frame at some frequency ω_ϕ. In this rotating frame, the equilibrium plasma rotation frequency is shifted to $\bar{\omega}_e(r) = \omega_e(r) - \omega_\phi$, and eigenmode frequencies are Doppler-shifted according to $\bar{\omega}_\alpha = \omega_\alpha - l\omega_\phi$. Then, it is well-known that canonical angular momentum takes the same value in both the rotating and lab frames, $\bar{P}_\theta = P_\theta$, and energy is shifted according to $\bar{E} = E - \omega_\phi P_\theta$.[23] These relations also follow directly from Eqs. (32) and (34). When these relations are applied to Eq. (45), we find that dynamical eigenmode energy transforms according to

$$\omega_\alpha \bar{E}_\alpha = \bar{\omega}_\alpha E_\alpha. \tag{46}$$

This relation is consistent with the well-known fact that $|E_\alpha/\omega_\alpha|$ is the classical action for a linear wave (the "number of quanta" in the mode), an invariant under frame transformations. Thus, for example, if we choose a frame rotating at the phase velocity $\omega_\phi = \omega_\alpha/l$ of a given mode α that has a nonzero value of l, then $\bar{\omega}_\alpha = 0$ and the mode energy in that rotating frame is $\bar{E}_\alpha = 0$.

V. NONLINEAR WAVE INTERACTIONS

The quadratic nature of nonlinearities in the cold fluid equations implies that the state $\boldsymbol{\chi}(\boldsymbol{r}, t) = (\delta n, \delta v_z)$ evolves according to an equation of the form

$$\frac{\partial \boldsymbol{\chi}}{\partial t} + \hat{\boldsymbol{L}} \cdot \boldsymbol{\chi} + \boldsymbol{N}(\boldsymbol{\chi}, \boldsymbol{\chi}) = 0, \tag{47}$$

where $\hat{\boldsymbol{L}}$ is the linear operator of Eq. (10) and $\boldsymbol{N}(\boldsymbol{\chi}, \boldsymbol{\chi})$ represents quadratically nonlinear terms in the perturbed functions:

$$\boldsymbol{N}(\boldsymbol{\chi}, \boldsymbol{\chi}) = \begin{pmatrix} \nabla \cdot (\delta n \delta \boldsymbol{v}) \\ \delta \boldsymbol{v} \cdot \nabla \delta v_z \end{pmatrix}. \tag{48}$$

Applying to Eq. (47) an eigenmode decomposition of the system state, Eq. (12), and taking an energy inner product with respect to the eigenmode $\boldsymbol{\psi}_\alpha(\boldsymbol{r})$, results in a set of coupled quadratically nonlinear ordinary differential equations for the time dependence of the amplitudes $a_\alpha(t)$ appearing in Eq. (12)

$$E_\alpha(\dot{a}_\alpha + i\omega_\alpha a_\alpha) + \sum_{\beta,\gamma} C_{\alpha,\beta,\gamma} a_\beta a_\gamma = 0, \tag{49}$$

where $E_\alpha = \langle \boldsymbol{\psi}_\alpha, \boldsymbol{\psi}_\alpha\rangle$, and the nonlinear coupling coefficient $C_{\alpha,\beta,\gamma} = \langle \boldsymbol{\psi}_\alpha, \boldsymbol{N}(\boldsymbol{\psi}_\beta, \boldsymbol{\psi}_\gamma)\rangle_E$.

Equation (49) is an elegant and complete description of the nonlinear coupling between modes in the ideal cold fluid equations. When mode α is a dynamical eigenmode, E_α is the energy of the eigenmode. When $\boldsymbol{\psi}_\alpha$ is an equilibrium eigenmode, Eq. (49) describes the nonlinear evolution of the equilibrium.

When mode α is a discrete dynamical eigenmode, the nonlinear coupling coefficient can be written as

$$C_{\alpha,\beta,\gamma} = \frac{1}{2}\int d^3r \frac{\omega_\alpha}{\hat{\omega}_\alpha}\left[m n_e \delta v_{z,\alpha}^* \delta \boldsymbol{v}_\beta \cdot \nabla \delta v_{z,\gamma} + e\delta\phi_\alpha^* \nabla \cdot (\delta n_\beta \delta \boldsymbol{v}_\gamma)\right] \tag{50}$$

using Eqs. (48) and (43), and the eigenmode energy E_α can be expressed as

$$E_\alpha = \frac{1}{2}\int d^3r \frac{\omega_\alpha}{\hat{\omega}_\alpha}\left[m n_e |\delta v_{z,\alpha}|^2 + e\delta\phi_\alpha^* \delta n_\alpha\right], \tag{51}$$

see Eq. (44).

In Sec. VI A, we will use these relations to analyze the experimental results presented in Sec. II.

VI. MODE-COUPLING EXPLANATION FOR THE EXPERIMENTS

We will now show that the observed frequency pattern in Fig. 2 can be explained as a 4-wave interaction between the diocotron mode and 3 nearly degenerate magnetized plasma waves, which are mode-coupled and mixed by the much lower-frequency diocotron mode. The 3 nearly degenerate waves in this example all have axial wavelengths $k_z = \pi/L$. Their parameters are as follows:

(1) an $l = 0, m_r = 2, m_z = 1$ TG plasma wave with (positive) frequency ω_0. This is the TG wave that is observed in Fig. 2 before the diocotron mode is launched at $t = 30$ s.
(2) an $l = +2, m_r = 1, m_z = 1$ TG plasma wave with frequency $\omega_2 > 0$ (i.e., a mode with positive azimuthal phase velocity).
(3) an $l = -2, m_r = 1, m_z = 1$ TG plasma wave and frequency $\omega_{-2} > 0$ (i.e., a mode with negative azimuthal phase velocity).

The mode numbers (m_r, l, m_z) are identified by comparing the observed frequencies to theory, and then by checking their correct z dependence and θ symmetry, comparing signals from the walls at different z positions (G5 and G8) and different sectors on electrodes S4 and S7. The radial dependence of the perturbed potential in these three waves is plotted in Fig. 7, obtained using a shooting solution of Eq. (18) for the electron plasma density profile used in the experiment (see Fig. 5). The length $L = 34.9$ cm was chosen to match the observed frequency $\omega_0/(2\pi) = 933$ kHz of the $l = 0, m_r = 2$ plasma wave just before the diocotron mode was launched (see Fig. 2). This "effective length"[27] for the mode corresponds closely to the estimated plasma length of 34 cm in the experiment. The theoretical frequencies of these 3 modes are also given in Fig. 7. The shooting method for the $l = 2$ diocotron mode itself (see Fig. 4) gives a mode frequency of $\omega_D/(2\pi) = 16.5$ kHz, close to the observed frequency (see Fig. 3).

Note that the three magnetized plasma eigenmodes have nearly the same frequencies, around 900 kHz. This near-degeneracy is important in explaining the observed nonlinear coupling between the modes.

This degeneracy is due to a property of Bessel functions. Recall that Bessel functions appear in the Trivelpiece–Gould (TG) dispersion relation for waves in plasma columns with uniform density: see Eqs. (19)–(21). If one plots the even Bessel functions as shown in Fig. 8, multiplying them by $(-1)^{l/2}$, the functions nearly line up for a large argument. (A similar plot could be made for the odd Bessel functions.)

Now, the dispersion relation (20) implies that each Bessel zero for a given l has a correspondence to $\pm l$ plasma mode frequencies with a value of m_r given by the order of the Bessel zero, counting from the left side of Fig. 8. In particular, the second zero of $J_0(x)$ is close to the first zero of $J_2(x)$ (the circled pair of zeroes in Fig. 8), and this implies a near-degeneracy of the $l = 0, m_r = 2$ mode with the $l = \pm 2, m_r = 1$ modes.

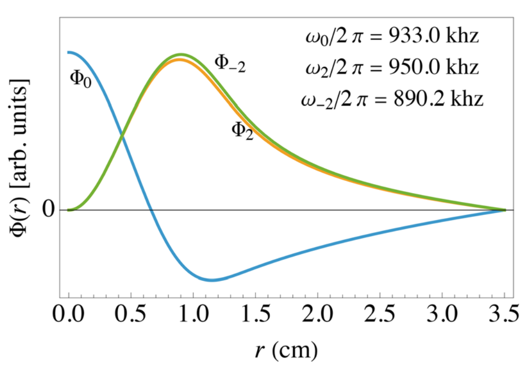

FIG. 7. Solid lines: Cold fluid theory for the perturbed potentials $\Phi_l(r)$ (in arbitrary units) and frequencies ω_l for the three plasma eigenmodes participating in the mode-coupling occurring in Fig. 2, where l is the azimuthal mode number of the modes. The eigenmodes and frequencies are obtained using the shooting method solutions of Eq. (18), for equilibrium density and rotation frequency given in Fig. 5.

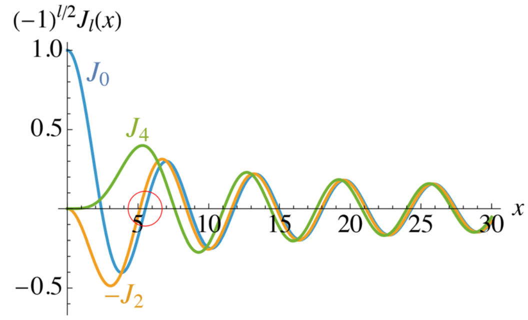

FIG. 8. The even Bessel functions $J_0(x)$, $-J_2(x)$, and $J_4(x)$. The circled zeroes correspond to the nearly degenerate mode frequencies responsible for the frequency pattern shown in Fig. 2.

While the experimental density profile is not uniform (see Fig. 5), it is close enough so that this near-degeneracy still occurs. The near-degeneracy causes strong mode coupling in the presence of the low frequency $l = 2$ diocotron pump wave, and the mode coupling produces noticeable frequency shifts (avoided crossings) that depend on the diocotron amplitude.

It is also important to note that one normally would not be able to pickup or excite $l \neq 0$ plasma modes using the cylindrically symmetric wall electrodes employed in these experiments. However, the $l = 2$ diocotron mode mixes the $l = \pm 2$ magnetized plasma modes with the $l = 0$ plasma mode, allowing them to be excited and picked up by the cylindrical electrodes. This is why three frequencies appear when the diocotron mode is excited—they correspond to three mixed eigenmodes that are different linear combinations of $l = \pm 2$ and $l = 0$, with only the $l = 0$ component of each linear combination observed.

One can see in Fig. 8 that there are more near-degeneracies at larger m_r values. For example, the three clustered zeroes just to the

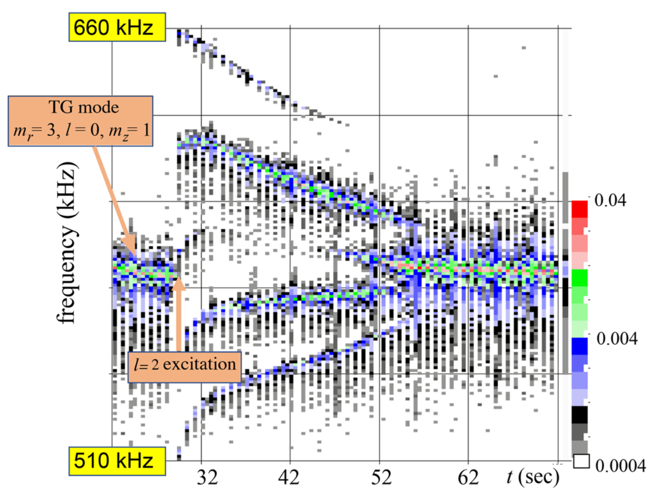

FIG. 9. Same experiment as in Fig. 2, except that now an $l = 0, m_r = 3, m_z = 1$ plasma mode is launched. As before, an $l = 2$ diocotron mode is also launched at $t = 30$ s after plasma creation, resulting in a pattern of 5 frequencies that converge as the diocotron mode decays. Adapted from Ref. 8.

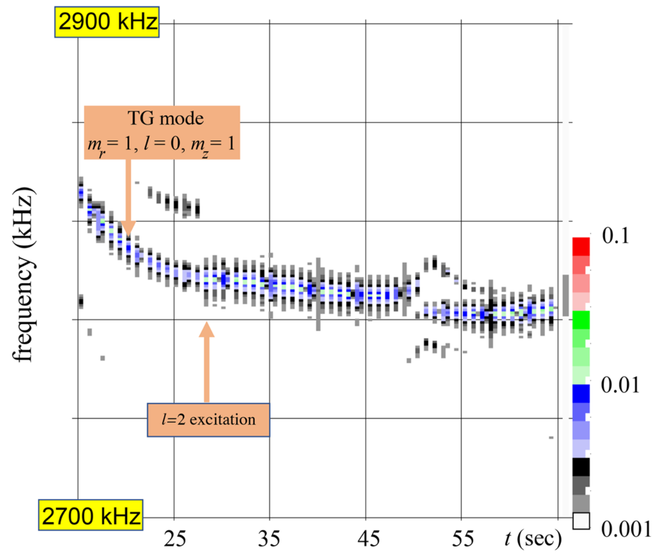

FIG. 10. Same experiment as in Fig. 2, except that now an $l = 0, m_r = 1, m_z = 1$ plasma mode is launched. An $l = 2$ diocotron mode is also launched at $t = 28$ s. The diocotron mode has no effect on the observed frequency spectrum. Adapted from Ref. 8.

right of the circle in Fig. 8 predict that an $l = 0, m_r = 3$ plasma mode will be nearly degenerate with four other plasma modes, $l = \pm 2, m_r = 2$ and $l = \pm 4, m_r = 1$, all with the same m_z value. The frequency splitting corresponding to this high-order degeneracy has also been observed (Fig. 9). In this experiment, an $l = 0, m_r = 3, m_z = 1$ mode is launched by lowering the excitation frequency Ω. At $t = 30$ s, an $l = 2$ diocotron mode is also launched, and in this case, the received spectrum splits into five peaks, corresponding to the expected number of near-degenerate plasma modes.

On the other hand, for the $l = 0, m_r = 1$ plasma mode, which corresponds to the first Bessel zero (before the circled zeros in Fig. 8), there are no near-degeneracies. When this wave is launched and a diocotron wave is added, there is no observed frequency splitting; see Fig. 10. This "control experiment" is more evidence that the observed frequency spectra can be explained by nonlinear mode coupling of near-degenerate plasma waves.

Furthermore, the frequency shifts and the relative strengths of modes in the spectra can be predicted quantitatively using our mode-coupling theory, i.e., Eq. (49). As an example, we consider the data in Fig. 2.

A. Quantitative mode-coupling analysis of Fig. 2

Following Eq. (12) and working in the rotating frame of the diocotron mode, we write the state vector for the mode-coupling process occurring in Fig. 2 in terms of the relevant eigenmodes,

$$\boldsymbol{\chi}(\boldsymbol{r}, t) = A\boldsymbol{\psi}_D(\boldsymbol{r}) + a_0(t)\boldsymbol{\psi}_0(\boldsymbol{r}) + a_2(t)\boldsymbol{\psi}_2(\boldsymbol{r}) + a_{-2}(t)\boldsymbol{\psi}_{-2}(\boldsymbol{r}) + \text{c.c.}, \tag{52}$$

where the term proportional to A is the $l = 2$ diocotron eigenmode, labeled "D," and the other three terms in the sum are the three magnetized plasma eigenmodes labeled by their azimuthal mode numbers $l = -2, 0$, and 2. These three modes are standing waves in z of the form given by Eq. (15), with positive frequencies ω_l and all with axial wavenumber $k_z = \pi/L$. The complex conjugate eigenmodes are also included in Eq. (52) in order to produce a real state vector.

We now evaluate the nonlinear mode-coupling equation, Eq. (49), for the state vector given in Eq. (52), which describes the plasma wave evolution shown in Fig. 2. It is useful to work in the frame of the diocotron mode, and take the diocotron amplitude A real, so that the mode is a stationary perturbation to the plasma shape, making the plasma cross section elliptical with a density perturbation proportional to $2A\cos(2\theta)$. The complex plasma wave amplitudes $a_l(t)$ are assumed to be small compared to A, so in Eq. (49), we drop nonlinear terms in the a_l s, but keep nonlinear coupling to the diocotron mode to first order in A. Then, Eq. (49) can be evaluated for the time evolution of each amplitude a_l. Selection rules in azimuthal mode number l eliminate many nonlinear cross terms, leaving

$$(\dot{a}_0 + i\omega_0 a_0)\bar{E}_0 + A(a_2 C_{0,2} + a_{-2}C_{0,-2}) = 0, \tag{53}$$

$$(\dot{a}_2 + i\bar{\omega}_2 a_2)\bar{E}_2 + A a_0 C_{2,0} = 0, \tag{54}$$

$$(\dot{a}_{-2} + i\bar{\omega}_{-2} a_{-2})\bar{E}_{-2} + A a_0 C_{-2,0} = 0, \tag{55}$$

where $\bar{E}_l = \langle \boldsymbol{\psi}_l, \boldsymbol{\psi}_l \rangle_{\bar{E}}$ is the energy of eigenmode l, the bars on the frequencies and energies indicate that they are evaluated in the rotating frame of the diocotron mode, and the coupling coefficients $C_{l,l'}$ are

$$C_{0,2} = \bar{C}_{0,D^*,2} + \bar{C}_{0,2,D^*}, \tag{56}$$

$$C_{0,-2} = \bar{C}_{0,D,-2} + \bar{C}_{0,-2,D}, \tag{57}$$

$$C_{2,0} = \bar{C}_{2,D,0} + \bar{C}_{2,0,D}, \tag{58}$$

$$C_{-2,0} = \bar{C}_{-2,D^*,0} + \bar{C}_{-2,0,D^*}, \tag{59}$$

where $\bar{C}_{\alpha,\beta,\gamma}$ refers to nonlinear coupling coefficients in Eq. (49) evaluated in the rotating frame of the diocotron mode, and the subscript D^* refers to the complex conjugate diocotron eigenmode in Eq. (52), proportional to $\exp(-2i\theta)$ and with negative frequency $-\omega_D$.

It should be noted that we have simplified Eqs. (54) and (55) by dropping a nonlinear coupling term proportional to Aa_0^* that appears in both equations, and we have similarly simplified Eq. (53) by dropping terms proportional to Aa_2^* and Aa_{-2}^*. These terms are negligible compared to those kept, because the natural frequencies of the complex-conjugate modes are negative, and so they are far from resonance with the positive frequency magnetized plasma eigenmodes described by Eqs. (53)–(55).

Equations (53)–(55) are linear in the daughter amplitudes and have constant coefficients, so an eigenmode solution proportional to $\exp(-i\bar{\omega}t)$ is possible. This converts the equations into the matrix eigenvalue problem

$$-i\bar{\omega}\begin{pmatrix} a_0 \\ a_2 \\ a_{-2} \end{pmatrix} + \boldsymbol{M}\cdot\begin{pmatrix} a_0 \\ a_2 \\ a_{-2} \end{pmatrix} = \boldsymbol{0}, \tag{60}$$

where

$$\boldsymbol{M} = \begin{pmatrix} i\omega_0 & AC_{0,2}/\bar{E}_0 & AC_{0,-2}/\bar{E}_0 \\ AC_{2,0}/\bar{E}_2 & i\bar{\omega}_2 & 0 \\ AC_{-2,0}/\bar{E}_{-2} & 0 & i\bar{\omega}_{-2} \end{pmatrix}. \tag{61}$$

Let us first consider the solutions of this matrix eigenvalue problem in the infinite magnetic field limit, where $\bar{\omega}_{-2} = \bar{\omega}_2 = \omega_2$, $\Phi_{-2}(r) = \Phi_2(r)$, $\bar{E}_{-2} = \bar{E}_2$, $C_{0,-2} = C_{0,2}$, and $C_{-2,0} = C_{2,0}$.

The form of mode coupling for infinite B is similar to what occurs for drumhead modes of a slightly elliptical drumhead.[37] These drumhead modes are standing waves in θ that are either even or odd in θ. The $\cos 2\theta$ perturbation to the drumhead shape causes mode coupling and frequency shifts for those drumhead modes that are even in θ (corresponding to the upper and lower frequencies seen in Fig. 2). This is classic avoided crossing behavior for two near-degenerate modes that are coupled by a perturbation.[38] However, no mode coupling or shifts occur for an odd drumhead mode (corresponding to the almost unshifted central frequency in Fig. 2), because the odd mode does not couple to the even perturbation (to lowest order in the perturbation amplitude A). This simplified summary is fleshed out below.

For $B = \infty$, the characteristic polynomial following from Eqs. (60) and (61) can be factored, yielding:

$$(\bar{\omega} - \omega_2)\left(\bar{E}_0 \bar{E}_2 (\bar{\omega}^2 - \bar{\omega}(\omega_0 + \omega_2) + \omega_0 \omega_2) + 2A^2 C_{0,2} C_{2,0}\right) = 0. \quad (62)$$

There are three solutions to Eq. (62) for the perturbed eigenmode frequency $\bar{\omega}$, which we label $\bar{\omega}^+, \bar{\omega}^-$, and $\bar{\omega}^c$, standing for the upper, lower, and center frequencies observed in Fig. 2. At infinite magnetic field, the center solution is $\bar{\omega}^c = \omega_2$, unmodified by the diocotron pump wave. The associated eigenvector is $(a_0, a_2, a_{-2}) = (0, 1, -1)$. This corresponds to a potential eigenfunction $\delta\phi^c(\boldsymbol{r}, t) = e^{-i\omega_2 t}\Phi_2(r) \sin 2\theta \cos(k_z z)$. The mode does not couple to the diocotron pump wave because the eigenfunction has odd symmetry in θ while the diocotron mode, proportional to $\cos 2\theta$, has even symmetry, and this explains why there is no frequency shift for this mode at the order in A to which we are working. Because the mode is odd, there is also no mode coupling to $l = 0$, so this mode would not be picked up or excited by the cylindrically symmetric electrodes used in the experiment (if the magnetic field were actually infinite). For a large but finite magnetic field, there is weak coupling to this mode because it is no longer exactly of the $\sin 2\theta$ form, and this explains the relatively weak, almost unshifted, signal for the central mode in Fig. 2.

The upper and lower eigenmode solutions satisfy the quadratic equation within Eq. (62), yielding the two solutions

$$\bar{\omega}^{\pm} = \frac{\omega_0 + \omega_2}{2} \pm \frac{1}{2}\sqrt{(\omega_2 - \omega_0)^2 - 8A^2 C_{0,2} C_{2,0}/(\bar{E}_0 \bar{E}_2)}. \quad (63)$$

These frequencies are real because the eigensystem is stable with $\bar{E}_0 \bar{E}_2 > 0$ and $C_{0,2}C_{2,0} < 0$ (as we will see later). From Eq. (63), one can see that strong frequency splitting in the avoided crossing occurs when the detuning between near-degenerate modes, $|\omega_0 - \omega_2|$, is smaller than the nonlinear coupling term $A\sqrt{8|C_{0,2}C_{2,0}/(\bar{E}_0\bar{E}_2)|}$.

The corresponding eigenvectors for the upper and lower modes are $(a_0, a_2, a_{-2}) = (c_\pm, 1, 1)$ where $c_\pm = (\omega_2 - \omega_0 \mp s)\bar{E}_2/(2AC_{2,0})$, and s is the square root appearing in Eq. (63), a positive real number. These two eigenvectors correspond to potential eigenfunctions $\delta\phi^\pm$ of the form $\delta\phi^\pm(\boldsymbol{r}, t) = e^{-i\bar{\omega}^\pm t}(c_\pm \Phi_0(r) + 2\cos 2\theta \Phi_2(r))\cos(k_z z)$. For the infinite magnetic field case used here, these two perturbed eigenmodes are standing waves that are even in θ, and therefore couple to the diocotron mode. Also, these eigenmodes have an $l = 0$ component that can easily be picked up using the cylindrically symmetric wall electrodes. Equation (63) implies that the frequency shifts for these two modes are equal and opposite around the average of the $l = 0$ and $l = 2$ unperturbed modes. For near degeneracy, where $\omega_0 \approx \omega_2$, the positive and negative frequency shifts scale roughly as pump amplitude A, and have roughly equal magnitude $l = 0$ components to be picked up on the wall, which is qualitatively what is observed in the experiment for the upper and lower frequency features in the measured spectrum, Fig. 2.

To make more quantitative comparisons to the experimental data, we must evaluate the coupling coefficients and mode energies. Using Eqs. (50) and (56)–(59), we obtain

$$\begin{aligned}
C_{0,2} &= \frac{1}{2}\int d^3r \left[m n_e \delta v_{z,0}^* \delta \boldsymbol{v}_D^* \cdot \nabla \delta v_{z,2} + e\delta\phi_0^* \nabla \cdot (\delta n_D^* \delta \boldsymbol{v}_2 + \delta n_2 \delta \boldsymbol{v}_D^*) \right], \\
C_{0,-2} &= \frac{1}{2}\int d^3r \left[m n_e \delta v_{z,0}^* \delta \boldsymbol{v}_D \cdot \nabla \delta v_{z,-2} + e\delta\phi_0^* \nabla \cdot (\delta n_D \delta \boldsymbol{v}_{-2} + \delta n_{-2} \delta \boldsymbol{v}_D) \right], \\
C_{2,0} &= \frac{1}{2}\int d^3r \frac{\bar{\omega}_2}{\hat{\omega}_2} \left[m n_e \delta v_{z,2}^* \delta \boldsymbol{v}_D \cdot \nabla \delta v_{z,0} + e\delta\phi_2^* \nabla \cdot (\delta n_D \delta \boldsymbol{v}_0 + \delta n_0 \delta \boldsymbol{v}_D) \right], \\
C_{-2,0} &= \frac{1}{2}\int d^3r \frac{\bar{\omega}_{-2}}{\hat{\omega}_{-2}} \left[m n_e \delta v_{z,-2}^* \delta \boldsymbol{v}_D^* \cdot \nabla \delta v_{z,0} + e\delta\phi_{-2}^* \nabla \cdot (\delta n_D^* \delta \boldsymbol{v}_0 + \delta n_0 \delta \boldsymbol{v}_D^*) \right],
\end{aligned} \quad (64)$$

where $\hat{\omega}_{\pm 2} = \omega_{\pm 2} \mp 2\omega_e(r)$. To the lowest order in $1/B$, we can drop all $E \times B$ drift velocity terms. Applying Eqs. (15)–(17), the coupling coefficients then reduce to

$$C_{0,2} = C_{0,-2} = \frac{ie^2 k_z^2 c}{2mB}\int d^3r \frac{\partial n_e}{\partial r}\frac{\Phi_D(r)\Phi_0(r)\Phi_2(r)}{r\hat{\omega}_D(r)\omega_2}, \quad (65)$$

$$C_{2,0} = C_{-2,0} = \frac{ie^2 k_z^2 c}{2mB}\int d^3r \frac{\partial n_e}{\partial r}\frac{\Phi_D(r)\Phi_0(r)\Phi_2(r)}{r\hat{\omega}_D(r)\omega_0}, \quad (66)$$

where $\Phi_D(r), \Phi_0(r)$, and $\Phi_2(r)$ are the unperturbed diocotron, $l = 0$ plasma, and $l = 2$ plasma potentials, respectively, and $\hat{\omega}_D = \omega_D - 2\omega_e(r)$ is the diocotron frequency in the local plasma frame. Since the integrands in Eqs. (65) and (66) are real-valued, if there were an exact degeneracy with $\omega_0 = \omega_2$, the coupling coefficients would satisfy $C_{0,2} = -C_{2,0}^*$, so that $C_{0,2}C_{2,0} < 0$, as we stated previously. This inequality remains true for $\omega_0 \neq \omega_2$ and for large but finite magnetic field (i.e., where the drift approximation is valid).

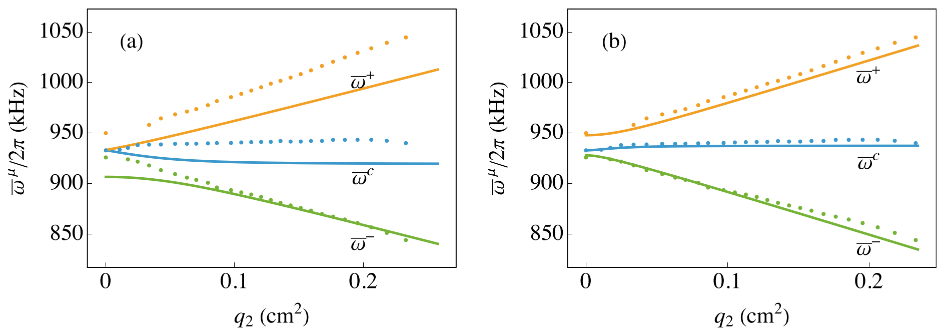

FIG. 11. Observed frequencies (dots) corresponding to the spectrogram in Fig. 2, and theoretical perturbed TG eigenmode frequencies $\bar{\omega}^+$, $\bar{\omega}^-$, and $\bar{\omega}^c$ (solid lines), vs quadrupole moment q_2 of the diocotron mode shown in Fig. 3. In (a), the unperturbed (i.e., $q_2 = 0$) mode frequencies ω_0, ω_2, and ω_{-2} used in Eq. (61) are the cold fluid theory predictions given in Fig. 7. In (b), 14.5 kHz is added to $\omega_2/2\pi$, and 21.3 kHz is added to $\omega_{-2}/2\pi$, so as to agree with experimental measurement of these unperturbed frequencies.

The mode energies are

$$\begin{aligned}\bar{E}_0 &= \frac{1}{2}\int d^3r\left(mn_e|\delta v_{z,0}|^2 + e\delta\phi_0^*\delta n_0\right)\\ &= \frac{1}{16\pi}\int d^3r\left\{\left[\frac{\partial\Phi_0}{\partial r}\right]^2 + k_z^2\left[1+\frac{\omega_p^2}{\omega_0^2}\right]\Phi_0^2\right\},\end{aligned} \tag{67}$$

$$\begin{aligned}\bar{E}_{\pm2} &= \frac{1}{2}\int d^3r\frac{\bar{\omega}_{\pm2}}{\hat{\omega}_{\pm2}}\left(mn_e|\delta v_{z,\pm2}|^2 + e\delta\phi_{\pm2}^*\delta n_{\pm2}\right)\\ &\simeq \frac{1}{16\pi}\int d^3r\left\{\left[\frac{\partial\Phi_2}{\partial r}\right]^2 + \left[\frac{4}{r^2}+k_z^2\left(1+\frac{\omega_p^2}{\omega_2^2}\right)\right]\Phi_2^2\right\},\end{aligned} \tag{68}$$

where the second form in Eq. (68) is for an infinite magnetic field. The energies are manifestly positive and therefore $\bar{E}_0\bar{E}_2 > 0$, as stated previously in relation to Eq. (63).

We use the calculated mode energies and coupling coefficients from Eqs. (64), (67) and (68) to solve for the perturbed mode frequencies $\bar{\omega}^+$, $\bar{\omega}^-$, and $\bar{\omega}^c$, finding the roots of the cubic characteristic polynomial arising from the eigenvalue problem of Eq. (60). The resulting frequencies are compared to the measured frequency spectrum in Fig. 11(a), plotted vs the quadrupole moment q_2 of the diocotron mode,

$$q_2 = |\langle r^2\exp(-2i\theta)\rangle| = AN^{-1}\left|\int d^3r\exp(-2i\theta)r^2\delta n_D(\boldsymbol{r},t)\right|,$$

where here $\langle\cdot\rangle$ is an average over the plasma density, and N is the total particle number. In the experiment, the quadrupole moment is determined from the magnitude of the diocotron wall signal (Fig. 3), which is proportional to q_2. This q_2 measurement is calibrated by comparing the wall signal to a direct measurement of q_2 via dumps of the plasma onto the phosphor screen for several diocotron mode amplitudes, determining the constant of proportionality between the wall signal and q_2. The theoretical frequency splitting in Fig. 11(a) is similar to that observed in the experiment.

A careful reader might notice that in Fig. 11(a) the theory frequencies for $\bar{\omega}^+$ and $\bar{\omega}^-$ as $q_2 \to 0$ do not match those predicted for $\omega_{\pm2}$ given in Fig. 7. This is because these two eigenmodes have frequencies $\bar{\omega}^+$ and $\bar{\omega}^-$ when viewed in the rotating frame of the diocotron mode, but in the laboratory frame, each perturbed eigenmode exhibits three separate frequencies caused by Doppler shifts, one for each azimuthal mode number making up the mode. The perturbed potential in the upper and lower frequency eigenmodes takes the lab frame form

$$\begin{aligned}\delta\phi^\pm(\boldsymbol{r},t) = &\left(a_0e^{-i\bar{\omega}^\pm t}\Phi_0(r) + a_2e^{-i(\bar{\omega}^\pm+\omega_D)t+2i\theta}\Phi_2(r)\right.\\ &\left.+a_{-2}e^{-i(\bar{\omega}^\pm-\omega_D)t-2i\theta}\Phi_{-2}(r)\right)\cos(k_zz) + \text{c.c.}.\end{aligned} \tag{69}$$

The only azimuthal component studied in these experiments and plotted in Fig. 11(a) is the $l = 0$ component, with frequencies $\bar{\omega}^\pm \to \bar{\omega}_{\pm2} = \omega_{\pm2}\mp\omega_D$ as $A \to 0$; see Eqs. (54) and (55). These Doppler shifts due to diocotron mode rotation account for the shifted frequencies in Fig. 11(a) as $q_2 \to 0$. Also, Eq. (69) shows that the $l = \pm2$ components of these two eigenmodes approach the expected frequencies as $A \to 0$: $\bar{\omega}^+ + \omega_D \to \omega_2$ and $\bar{\omega}^- - \omega_D \to \omega_{-2}$.

A better fit between theory and experiment can be obtained by allowing a small adjustment to the frequencies $\omega_{\pm2}$ of the unperturbed $l = \pm2$ plasma modes when evaluating the matrix $\boldsymbol{M}$ in Eq. (61), without changing the other matrix coefficients. Recall that ω_0 was already matched to the experimental measurement, but the unperturbed frequencies $\omega_{\pm2}$ were also measured in the experiment and so could also be matched. The measured $l = 2$ mode frequency, 964.5 kHz, was 14.5 kHz higher than the prediction given in Fig. 7, and the measured $l = -2$ mode frequency, 911.5 kHz, was 21.3 kHz higher, presumably because the effective length L for these modes[27] is slightly smaller than that for the $l = 0$ mode. Adding these corrections to the $l = \pm2$ unperturbed theory frequencies yield a much better fit to the perturbed eigenmode frequencies, shown in Fig. 11(b). The theoretical perturbed frequencies in the presence of the diocotron mode are now almost identical to the frequencies in the experiment.

The relative amplitudes of the eigenmodes can also be predicted. The modes are driven with a cylindrically symmetric external potential $\phi_{ext}(r,z,t)$ created by applying $N_{cycle} = 5$ cycles at a frequency of $\Omega/(2\pi) = 930$ kHz to a cylindrically symmetric wall electrode. Equation (47) then has a driving term,

$$\frac{\partial\boldsymbol{\chi}}{\partial t} + \hat{\boldsymbol{L}}\cdot\boldsymbol{\chi} + \boldsymbol{N}(\boldsymbol{\chi},\boldsymbol{\chi}) + \boldsymbol{f}(r,z,t) = 0, \tag{70}$$

where $\boldsymbol{f} = (0, (e/m)\partial\phi_{ext}/\partial z)$. This adds a driving term to Eq. (60), which becomes

$$\frac{\partial}{\partial t}\begin{pmatrix} a_0 \\ a_2 \\ a_{-2} \end{pmatrix} + \boldsymbol{M}\cdot\begin{pmatrix} a_0 \\ a_2 \\ a_{-2} \end{pmatrix} + \begin{pmatrix} f(t) \\ 0 \\ 0 \end{pmatrix} = 0, \tag{71}$$

where $f(t) = \langle \boldsymbol{\psi}_0, \boldsymbol{f}\rangle_{\bar{E}}/\bar{E}_0$. These coupled linear equations can be solved using the eigenvalues and eigenvectors of the matrix $\boldsymbol{M}$. Introducing the notation $\boldsymbol{a} = (a_0, a_2, a_{-2})$, the solution for $\boldsymbol{a}(t)$ can be written in the form

$$\boldsymbol{a} = \sum_{\mu} \alpha_\mu(t)\boldsymbol{e}^\mu, \tag{72}$$

where $\boldsymbol{e}^\mu$ are the right eigenvectors of $\boldsymbol{M}$, with index $\mu = +, -,$ or c, and with corresponding eigenvalues $i\bar{\omega}^\mu(A)$. The coefficients $\alpha^\mu(t)$ satisfy the uncoupled ODEs,

$$\dot{\alpha}^\mu + i\bar{\omega}^\mu\alpha^\mu + \frac{\boldsymbol{e}_L^\mu}{\boldsymbol{e}_L^\mu\cdot\boldsymbol{e}^\mu}\cdot\begin{pmatrix} f(t) \\ 0 \\ 0 \end{pmatrix} = 0, \tag{73}$$

where $\boldsymbol{e}_L^\mu$ are the left eigenvectors of $\boldsymbol{M}$. Once the forcing function $f(t)$ has turned off (i.e., after the five cycles of applied wall voltage), the solution of Eq. (73) can be written in terms of the Fourier transform $\tilde{f}(\omega)$ of the forcing function $f(t)$,

$$\alpha^\mu = -\frac{\boldsymbol{e}_L^\mu}{\boldsymbol{e}_L^\mu\cdot\boldsymbol{e}^\mu}\cdot\begin{pmatrix} \tilde{f}(\bar{\omega}^\mu) \\ 0 \\ 0 \end{pmatrix} e^{-i\bar{\omega}^\mu t}. \tag{74}$$

The $l = 0$ component of the potential $\delta\phi(\boldsymbol{r}, t)$ is then picked up on a receiving wall electrode at $r = r_w$, through the resulting induced image charge. Using Eqs. (15), (52), (72), and (74), the $l = 0$ potential is

$$\delta\phi_0(r, z, t) = -\Phi_0(r)\cos(k_z z)\sum_\mu \frac{e_{L1}^\mu e_1^\mu \tilde{f}(\bar{\omega}^\mu)}{\boldsymbol{e}_L^\mu\cdot\boldsymbol{e}^\mu}e^{-i\bar{\omega}^\mu t} + \text{c.c.}, \tag{75}$$

where the subscript 1 stands for the first component (the $l = 0$ component) of the eigenvectors. Thus, the strength of each frequency $\bar{\omega}^\mu$ in the received signal is proportional to the dimensionless factor

$$s^\mu \equiv \left\| \frac{e_{L1}^\mu e_1^\mu \tilde{f}(\bar{\omega}^\mu)}{\boldsymbol{e}_L^\mu\cdot\boldsymbol{e}^\mu} \right\|. \tag{76}$$

The Fourier transform of $f(t)$ has frequency dependence given by

$$\tilde{f}(\omega) = f_0\frac{e^{i2\pi N_{cycle}\omega/\Omega} - 1}{\omega^2 - \Omega^2}, \tag{77}$$

for some complex constant f_0. The resulting signal strengths s^μ are plotted vs the diocotron mode quadrupole moment q_2 in Fig. 12. The curves labeled $+, -, c$ correspond, respectively, to the upper, lower, and center frequencies in the data of Figs. 2 and 11. Dots are measured values of the signal strength in arbitrary units. The theory is adjusted by a single overall amplitude factor for all three curves to best match the data. Changing the frequencies of the unperturbed modes by as little as a few kilohertz has a noticeable effect on the shapes of the theory curves; we used the same measured frequency values here for ω_0, ω_2, and ω_{-2} as were used in Fig. 11(b).

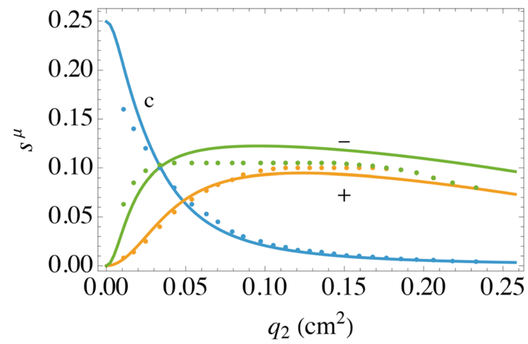

FIG. 12. Dimensionless strengths s^μ of the three frequencies $\bar{\omega}^\mu$, observed in Figs. 2 and 11, vs diocotron quadrupole moment q_2, where the index μ takes values $\mu = +, -,$ or c (upper, lower, or central frequency, respectively). Dots: experimental measurements; curves: Eq. (76).

For a larger diocotron quadrupole moment q_2 the top and bottom frequencies (curves + and −) have nearly constant strength, falling off somewhat as q_2 increases and the frequencies diverge from the peak of $\tilde{f}(\omega)$. The central frequency feature (curve c) has a strongly decreasing strength with increasing q_2, in good agreement with the measurements. As we discussed previously, the eigenmode corresponding to the central frequency is close to an odd standing wave in θ (when viewed in the rotating frame of the diocotron mode) and therefore does not couple well to the even-in-θ perturbation of the diocotron mode. Evidently, as the diocotron amplitude increases and the plasma cross section becomes more elliptical, this mode becomes more like this odd standing wave; while for small diocotron amplitude, it approaches the original unperturbed $l = 0$ plasma wave.

VII. DISCUSSION

In this paper, we report on experiments using a pure electron plasma column, in which strong frequency shifts and mode coupling were induced in several near-degenerate plasma modes, caused by the excitation of a relatively low-frequency diocotron wave. This wave caused the plasma column to have a slightly elliptical cross section, and the observed mode-coupling and frequency shifts could be qualitatively understood as being similar to the avoided crossings induced in the standing waves of a slightly elliptical drumhead. These effects were amplified by the near-degeneracy of the plasma modes, which was shown to be related to a close correspondence between Bessel functions of even index and large argument. The near degeneracies produced strong mode coupling and frequency shifts in the frequency spectra of up to five plasma waves when they were launched simultaneously with an $l = 2$ diocotron mode.

The dependence of the mode frequency shifts on the amplitude of the diocotron mode and the strength of the different observed plasma wave signals were explained in detail by a cold fluid theory of the nonlinear mode coupling between the waves. The theory employed a novel approach in which mode-coupling coefficients were evaluated using an inner product based on the wave energy. This inner product has the useful property that the linear eigenmodes of the system are orthogonal with respect to it, which greatly simplifies the mode-coupling theory. The theory makes use of, and clarifies, the deep connection between conserved dynamical quantities and the Hermitian (or anti-Hermitian) properties of the linearized system. The approach is quite general and could be applied to any ideal (energy and/or momentum conserving) set of fluid or plasma equations.

In the experiments considered here, the mode coupling induced by the diocotron pump wave produced frequency shifts but did not induce wave instabilities. However, in several other experiments, we have observed various nonlinear instabilities induced by mode coupling. These instabilities can also be understood in detail using the formalism developed here. These nonlinear wave instability studies will be presented in forthcoming papers.

ACKNOWLEDGMENTS

The authors benefited from discussions with Professor T. M. O'Neil. Experimental work performed by visiting student Nicola Panzeri contributed to Figs. 2, 3, 9, and 10, and formed a portion of his Ph.D. thesis.[8] This work was supported by NSF Grant No. PHY2106332.

AUTHOR DECLARATIONS

Conflict of Interest

The authors have no conflicts to disclose.

Author Contributions

Daniel H. E. Dubin: Conceptualization (lead); Formal analysis (lead); Funding acquisition (lead); Investigation (lead); Methodology (lead); Project administration (lead); Writing – original draft (lead); Writing – review & editing (lead). **A. Kabantsev:** Conceptualization (supporting); Data curation (equal); Investigation (equal); Supervision (supporting); Validation (equal); Visualization (equal); Writing – review & editing (supporting). **C. F. Driscoll:** Project administration (supporting); Supervision (supporting); Writing – review & editing (supporting).

DATA AVAILABILITY

The data that support the findings of this study are available from the corresponding author upon reasonable request.

APPENDIX A: THE SPECTRAL THEOREM

Consider a linear operator $\hat{\boldsymbol{H}}$ that is Hermitian with respect to a class of functions $\{\boldsymbol{f}\}$ that satisfy some given homogeneous boundary conditions, and with respect to an inner product $\langle\cdot,\cdot\rangle$; i.e., for any functions $\boldsymbol{f}$ and $\boldsymbol{g}$ taken from this class, $\langle\boldsymbol{f},\hat{\boldsymbol{H}}\cdot\boldsymbol{g}\rangle = \langle\boldsymbol{g},\hat{\boldsymbol{H}}\cdot\boldsymbol{f}\rangle^*$. Let us further assume that the operator has eigenvalues ω_α and corresponding eigenfunctions $\boldsymbol{\psi}_\alpha$ that are members of the class $\{\boldsymbol{f}\}$, and are determined by the solution of the eigenvalue problem

$$\hat{\boldsymbol{H}}\cdot\boldsymbol{\psi}_\alpha = \omega_\alpha\boldsymbol{\psi}_\alpha. \tag{A1}$$

[In our paper, $\hat{\boldsymbol{H}} = -i\hat{\boldsymbol{L}}$.] Now, we will take an inner product of both sides of this equation with respect to another eigenfunction $\boldsymbol{\psi}_\beta$

$$\langle\boldsymbol{\psi}_\beta,\hat{\boldsymbol{H}}\cdot\boldsymbol{\psi}_\alpha\rangle = \omega_\alpha\langle\boldsymbol{\psi}_\beta,\boldsymbol{\psi}_\alpha\rangle. \tag{A2}$$

However, the Hermitian property of $\hat{\boldsymbol{H}}$ implies that the left-hand side of this expression can be replaced by

$$\langle\boldsymbol{\psi}_\alpha,\hat{\boldsymbol{H}}\cdot\boldsymbol{\psi}_\beta\rangle^* = \omega_\alpha\langle\boldsymbol{\psi}_\beta,\boldsymbol{\psi}_\alpha\rangle. \tag{A3}$$

Since $\hat{\boldsymbol{H}}\cdot\boldsymbol{\psi}_\beta = \omega_\beta\boldsymbol{\psi}_\beta$, the left-hand side reduces, yielding

$$\omega_\beta^*\langle\boldsymbol{\psi}_\alpha,\boldsymbol{\psi}_\beta\rangle^* = \omega_\alpha\langle\boldsymbol{\psi}_\beta,\boldsymbol{\psi}_\alpha\rangle, \tag{A4}$$

and this may be rewritten as

$$(\omega_\alpha - \omega_\beta^*)\langle\boldsymbol{\psi}_\beta,\boldsymbol{\psi}_\alpha\rangle = 0. \tag{A5}$$

Thus, if $\omega_\alpha \neq \omega_\beta^*$, then the two corresponding eigenmodes must be orthogonal. This is the first part of the spectral theorem for the eigenmodes of a Hermitian operator.

Now consider the case where we choose $\alpha = \beta$. Then, Eq. (A5) becomes

$$(\omega_\alpha - \omega_\alpha^*)\langle\boldsymbol{\psi}_\alpha,\boldsymbol{\psi}_\alpha\rangle = 0. \tag{A6}$$

If the eigenmode and inner product are such that $\langle\boldsymbol{\psi}_\alpha,\boldsymbol{\psi}_\alpha\rangle \neq 0$, then Eq. (A6) shows that the corresponding eigenvalue ω_α must be real. This is the second part of the spectral theorem.

Note that in our system, where the inner product is a generalized inner product, it is possible that $\langle\boldsymbol{\psi}_\alpha,\boldsymbol{\psi}_\alpha\rangle = 0$ in which case, it is also possible for the eigenvalue (i.e.,; the frequency) of the mode to be complex, indicating an exponential growth or decay of the mode amplitude. This is physically reasonable for our case, where the inner product of a mode is related to a conserved quantity, such as wave energy, proportional to the square of the amplitude. It is only possible for the mode to vary in amplitude while conserving this quantity if the quantity equals zero for that mode.

APPENDIX B: RELATIONS BETWEEN EULERIAN AND LAGRANGIAN VARIABLES, DERIVATION OF WAVE ENERGY AND ANGULAR MOMENTUM, AND AN INNER PRODUCT RELATION

We first discuss the equivalence of the Lagrangian equations of motion, Eqs. (26)–(29), to the Eulerian equations (6)–(8). For example, Eq. (28) is clearly equivalent to Eq. (7) once we add the definition of perturbed parallel fluid velocity,

$$\delta v_z = \hat{D}\delta z. \tag{B1}$$

Equations (26) and (27) can be derived through linearization of the r and θ components, respectively, of Eq. (3). Also, Eq. (29) is equivalent to Eq. (8). This follows from Eq. (6), which can be written as

$$\hat{D}\delta n + \hat{D}\delta r\frac{\partial n_e}{\partial r} + \frac{\partial}{\partial z}(n_e\hat{D}\delta z) = 0, \tag{B2}$$

after applying Eqs. (26) and (B1). Equation (B2) can then be integrated to yield

$$\delta n = -\delta r\frac{\partial n_e}{\partial r} - \frac{\partial}{\partial z}(n_e\delta z). \tag{B3}$$

Note that upon integration, one could add any function $f(r,z)$ to this expression for δn, but to be consistent with the other equations of motion $f(r,z)$ can only reflect a change to a slightly different equilibrium, which is ignored here. We therefore take $f = 0$.

This expression for the perturbed density can also be written as

$$\delta n = -\nabla \cdot (n_e \delta \boldsymbol{r}), \tag{B4}$$

proving the equivalence of Eqs. (8) and (29). Equations (B3) and (B4) are equivalent because

$$\nabla_\perp \cdot \delta \boldsymbol{r}_\perp \equiv \frac{1}{r}\frac{\partial}{\partial r}(r\delta r) + \frac{\partial \delta\theta}{\partial \theta} = 0, \tag{B5}$$

which can in turn be proven by applying $r^{-1}\frac{\partial}{\partial r} r$ to Eq. (26), and applying $\frac{\partial}{\partial \theta}$ to Eq. (27), which implies

$$\hat{D}\frac{1}{r}\frac{\partial}{\partial r} r\delta r = -\frac{\partial \omega_e}{\partial r}\frac{\partial \delta r}{\partial \theta} + \frac{c}{Br}\frac{\partial^2 \delta\phi}{\partial\theta\partial r}, \tag{B6}$$

$$\hat{D}\frac{\partial \delta\theta}{\partial \theta} = \frac{\partial \omega_e}{\partial r}\frac{\partial \delta r}{\partial \theta} - \frac{c}{Br}\frac{\partial^2 \delta\phi}{\partial\theta\partial r}. \tag{B7}$$

Adding Eqs. (B6) and (B7) together yields $\hat{D}\nabla_\perp \cdot \delta\boldsymbol{r}_\perp = 0$, which when integrated yields Eq. (B5) (again, dropping an arbitrary function of r and z after integration, for the same reason as before).

There is one more differential relation between the Lagrangian dynamical variables. Acting on Eq. (26) with $r\Omega_c \frac{\partial}{\partial z}$ and on Eq. (28) with $\frac{\partial}{\partial \theta}$, we find $\hat{D}\left(r\Omega_c \frac{\partial \delta r}{\partial z}\right) = -\hat{D}\frac{\partial \delta v_z}{\partial \theta}$, which upon integration yields the relation

$$r\Omega_c \frac{\partial \delta r}{\partial z} = -\frac{\partial \delta v_z}{\partial \theta}. \tag{B8}$$

This relation, together with Eqs. (8), (B4), and (B5), imply that only $\delta v_z(\boldsymbol{r}, t)$ and $\delta n(\boldsymbol{r}, t)$ need be specified at any time in order to determine the other Lagrangian variables $\delta r, \delta\theta, \delta z, \delta\phi$ at that time.

Next, we turn to the derivation of the wave energy E, Eq. (32), starting with Eq. (31). Evaluating this expression using Eq. (23) yields

$$E = \int d^3r \left[m n_e \delta\dot{z}\hat{D}\delta z - \frac{e n_e B}{c} r\delta r\delta\dot{\theta} - \mathscr{L} \right]. \tag{B9}$$

This equation can be further reduced by substituting for the Lagrangian density itself, Eq. (23), and for the time derivatives from Eqs. (B1) and (27), yielding

$$E = \int d^3r \left[\frac{1}{2} m n_e \delta v_z^2 - m n_e \omega_e \frac{\partial \delta z}{\partial \theta}\delta v_z + \frac{e n_e B}{c} r\delta r\omega_e \frac{\partial \delta\theta}{\partial\theta} + e n_e \delta\boldsymbol{r}\cdot\nabla\delta\phi - \frac{e n_e B}{2c}\frac{\partial \omega_e}{\partial r}\delta r^2 - \frac{|\nabla\delta\phi|^2}{8\pi} \right]. \tag{B10}$$

Integrating by parts on the second and fourth terms, applying Green's first identity to the sixth term, and using Eq. (B5) on the third term, produces

$$E = \int d^3r \left[\frac{1}{2} m n_e \delta v_z^2 + m n_e \omega_e \delta z \frac{\partial \delta v_z}{\partial \theta} - \frac{e n_e B}{c}\delta r\omega_e \frac{\partial}{\partial r}(r\delta r) - e\nabla\cdot(n_e\delta\boldsymbol{r})\delta\phi - \frac{e n_e B}{2c}\frac{\partial \omega_e}{\partial r}\delta r^2 + \frac{\delta\phi\nabla^2\delta\phi}{8\pi} \right] - \int_S d^2r \frac{\delta\phi\nabla\delta\phi}{8\pi}\cdot\hat{n}, \tag{B11}$$

where S is the surface of the surrounding electrodes and $\hat{n}$ is a unit vector normal to this surface. Assuming that these electrodes are held at their fixed equilibrium voltages, we can take $\delta\phi|_S = 0$ and this surface term in the energy can be dropped. We then substitute for $\frac{\partial \delta v_z}{\partial \theta}$ from Eq. (B8), use Eq. (B4) in the fourth term, apply Eq. (8) to the sixth term, and rewrite the third term to obtain

$$E = \int d^3r \left[\frac{1}{2} m n_e \delta v_z^2 - m n_e \omega_e \delta z r\Omega_c \frac{\partial \delta r}{\partial z} - \frac{e n_e B}{2cr}\omega_e \frac{\partial}{\partial r}(r\delta r)^2 + \frac{1}{2}e\delta n\delta\phi - \frac{e n_e B}{2c}\frac{\partial \omega_e}{\partial r}\delta r^2 \right]. \tag{B12}$$

We now integrate by parts on the second and third terms yielding

$$E = \int d^3r \left[\frac{1}{2} m n_e \delta v_z^2 + \frac{eB}{c}\omega_e r\delta r \frac{\partial}{\partial z}(n_e\delta z) + \frac{eB}{2c} r\delta r^2 \frac{\partial}{\partial r}(n_e\omega_e) + \frac{1}{2}e\delta n\delta\phi - \frac{e n_e B}{2c}\frac{\partial \omega_e}{\partial r}\delta r^2 \right]. \tag{B13}$$

We then apply Eq. (B3) to the second term, which allows us to combine the second, third, and fifth terms to yield Eq. (32).

Next, we derive the wave angular momentum P_θ, Eq. (34), starting from Eq. (33). Substituting for $\mathscr{L}$ from Eq. (23) yields

$$P_\theta = -\int d^3r \left[m n_e \frac{\partial \delta z}{\partial \theta}\hat{D}\delta z - \frac{e n_e B}{c} r\delta r \frac{\partial \delta\theta}{\partial \theta} \right]. \tag{B14}$$

This expression can be reduced in much the same way as the manipulations that led to our expression for wave energy, Eq. (32). We substitute for $\hat{D}\delta z$ from Eq. (B1) and for $\partial\delta\theta/\partial\theta$ from Eq. (B5), obtaining

$$P_\theta = -\int d^3r \left[m n_e \frac{\partial \delta z}{\partial \theta}\delta v_z + \frac{e n_e B}{c}\delta r \frac{\partial}{\partial r}(r\delta r) \right]. \tag{B15}$$

We then integrate by parts in θ on the first term, substitute from Eq. (B8), and rewrite the second term, yielding

$$P_\theta = -\frac{eB}{c}\int d^3r \left[n_e \delta z r \frac{\partial \delta r}{\partial z} + \frac{n_e}{2r}\frac{\partial}{\partial r}(r\delta r)^2 \right]. \tag{B16}$$

We then integrate by parts in r on the second term and in z on the first term, and apply Eq. (B3), yielding Eq. (34).

Finally, we derive a simplified form for the inner product $\langle \boldsymbol{\psi}_\alpha, \boldsymbol{\chi} \rangle$ when $\boldsymbol{\psi}_\alpha$ is a discrete dynamical eigenmode and $\boldsymbol{\chi} = (\delta n, \delta v_z)$ is any given state vector. Beginning with Eq. (42) and using Eq. (B3), we can rewrite δn_α^* in the angular momentum term as

$$\delta n_\alpha^* = -\frac{\partial}{\partial z}(n_e \delta z_\alpha^*) - \frac{\partial n_e}{\partial r}\delta r_\alpha^*, \tag{B17}$$

yielding

$$\langle \boldsymbol{\psi}_\alpha, \boldsymbol{\chi} \rangle_E = \frac{1}{2}\int d^3r \left[m n_e \delta v_{z,\alpha}^* \delta v_z + e\delta\phi_\alpha^* \delta n - \omega_e \frac{eBr}{c}\left(\delta r_\alpha^* \delta n - \delta r \frac{\partial}{\partial z}(n_e \delta z_\alpha^*) \right) \right]. \tag{B18}$$

We then integrate by parts on the z derivative term and apply Eq. (B8), obtaining

$$\langle \boldsymbol{\psi}_\alpha, \boldsymbol{\chi} \rangle_E = \frac{1}{2}\int d^3r \left[mn_e \delta v_{z,\alpha}^* \delta v_z + e\delta\phi_\alpha^* \delta n \right.$$
$$\left. - \omega_e \frac{eBr}{c}\left(\delta r_\alpha^* \delta n - \frac{n_e \delta z_\alpha^*}{\Omega_c r}\frac{\partial \delta v_z}{\partial \theta}\right)\right]. \tag{B19}$$

We now note that the eigenmode varies in θ as $\exp(il\theta)$, and that therefore only the Fourier component of $\boldsymbol{\chi}$ that also varies as $\exp(il\theta)$ contributes to the inner product, so we may replace $\partial\delta v_z/\partial\theta$ by $il\delta v_z$. Also, for a discrete dynamical eigenmode, Eq. (26) has the solution

$$\delta r_\alpha = -\frac{lc}{Br\hat{\omega}_\alpha}\delta\phi_\alpha, \tag{B20}$$

where $\hat{\omega}_\alpha = \omega_\alpha - l\omega_e(r)$, and Eq. (B1) implies that $\delta z_\alpha^* = -i\delta v_{z,\alpha}^*/\hat{\omega}_\alpha$. Applying these relations to Eq. (B19) leads directly to Eq. (43).

REFERENCES

[1] R. Z. Sagdeev and A. A. Galeev, *Nonlinear Plasma Theory* (W. A. Benjamin, New York, 1969), p. 5.
[2] R. C. Davidson, *Methods in Nonlinear Plasma Theory* (Academic Press, New York, 1972), Chap. VI.
[3] D. H. E. Dubin and T. M. O'Neil, "Trapped nonneutral plasmas, liquids, and crystals (the thermal equilibrium states)," Rev. Mod. Phys. **71**, 87 (1999).
[4] A. W. Trivelpiece and R. W. Gould, "Space charge waves in cylindrical plasma columns," J. Appl. Phys **30**, 1784 (1959).
[5] J. D. Jackson, *Classical Electrodynamics*, 3rd ed. (Wiley, New York, 1998), Sec. XIV B.
[6] R. H. Levy, "Diocotron instability in a cylindrical geometry," Phys. Fluids **8**, 1288 (1965); "Two new results in cylindrical diocotron theory," Phys. Fluids **11**, 920 (1968).
[7] D. H. E. Dubin, A. A. Kabantsev, and C. F. Driscoll, "Nonlinear beat wave decay of Kelvin/diocotron waves on a two-dimensional vortex," Phys. Fluids **36**, 034121 (2024).
[8] N. Panzeri, "Nonlinear wave excitation and interaction in pure electron plasmas," Ph. D. thesis (University of Milan, 2021).
[9] R. C. Davidson, *Physics of Nonneutral Plasmas* (Imperial College Press, London, 2001), p. 22.
[10] *ibid.* p. 290.
[11] F. Anderegg, "Internal transport in non-neutral plasmas," in *Physics with Trapped Charged Particles*, edited by M. Knoop, N. Madsen, and R. C. Thompson (Imperial College Press, London, 2014), pp. 195–218.
[12] J. H. Malmberg and C. F. Driscoll, "Long-time containment of a pure electron plasma," Phys. Rev. Lett. **44**, 654 (1980).
[13] M. Vergote, M. V. Schoor, Y. Xu, S. Jachmich, and R. Weynants, "The interplay between Reynolds stress and zonal flows: Direct numerical simulation as a bridge between theory and experiment," Plasma Phys. Controlled Fusion **48**, S75 (2006).
[14] J. Pedlosky, *Geophysical Fluid Dynamics*, 2nd ed. (Springer-Verlag, New York, 1987), Chap. VI.
[15] M. Z. Hasan and C. L. Kane, "Colloquium: Topological insulators," Rev. Mod. Phys. **82**, 3045 (2010).
[16] W. D. White, J. D. Malmberg, and C. F. Driscoll, "Resistive wall destabilization of diocotron waves," Phys. Rev. Lett. **49**, 1822 (1982).
[17] D. A. Schecter, D. H. E. Dubin, A. C. Cass, C. F. Driscoll, I. M. Lansky, and T. M. O'Neil, "Inviscid damping of asymmetries on a two-dimensional vortex," Phys. Fluids **12**, 2397 (2000).
[18] M. W. Anderson, T. M. O'Neil, D. H. E. Dubin, and R. W. Gould, "Degenerate mixing of plasma waves on cold, magnetized single-species plasmas," Phys. Plasmas **18**, 102113 (2011).
[19] A. G. Lieberman, "Mode excitation and propagation in waveguides containing anisotropic plasmas," Ph.D. thesis (CIT, Pasadena, 1964).
[20] S. H. Lamb, *Hydrodynamics* (Dover, New York, 1932). Chap. VIII.
[21] D. H. E. Dubin, *Numerical and Analytical Methods for Scientists and Engineers Using Mathematica* (John Wiley and Sons, Hoboken, NJ, 2003), Sec. IV. A 4.
[22] P. A. Sturrock, "In what sense do slow waves carry negative energy?," J. Appl. Phys. **31**, 2052 (1960).
[23] L. Landau and E. M. Lifshitz, *Mechanics*, 3rd ed. (Pergamon Press, New York, 1976), pp. 126–129.
[24] J. R. Danielson, D. H. E. Dubin, R. G. Greaves, and C. M. Surko, "Plasma and trap-based techniques for science with positrons," Rev. Mod. Phys. **87**, 247 (2015).
[25] R. C. Davidson, *Physics of Nonneutral Plasmas* (Imperial College Press, London, 2001), Chaps. IV and V.
[26] S. A. Prasad and T. M. O'Neil, "Waves in a cold pure electron plasma of finite length," Phys. Fluids **26**, 665 (1983).
[27] J. K. Jennings, R. L. Spencer, and K. C. Hansen, "Numerical calculation of axisymmetric electrostatic modes for cold finite-length nonneutral plasmas," Phys. Plasmas **2**, 2630 (1995).
[28] M. Case, "Stability of inviscid plane Couette flow," Phys. Fluids **3**, 143 (1960).
[29] D. H. E. Dubin, "Theory of electrostatic fluid modes in a cold spheroidal nonneutral plasma," Phys. Rev. Lett. **66**, 2076 (1991).
[30] S. Ramo "Space charge waves and field waves in an electron beam," Phys. Rev. **56**, 276 (1939); A. W. Trivelpiece, "Slow wave propagation in plasma waveguides," Ph. D. thesis (Caltech, 1958).
[31] *Handbook of Mathematical Functions*, 10th ed., edited by M. Abramowitz and I. Stegun (National Bureau of Standards, Washington, DC, 1972).
[32] G. B. Whitham, *Linear and Nonlinear Waves* (Wiley, New York, 1974), p. 390ff.
[33] H. Goldstein, C. P. Poole, and J. Safko, *Classical Mechanics*, 3rd ed. (Addison Wesley, New York, 2002), Chap. XIII.
[34] H. Kim, "Lagrangian description of warm plasmas," Report No. 470 (Stanford University Institute for Plasma Research, 1972).
[35] P. C. Shields, *Elementary Linear Algebra*, 2nd ed. (Worth, New York, 1973), pp. 274–280.
[36] R. Courant and D. Hilbert, *Methods of Mathematical Physics* (Wiley Interscience, New York, 1953), Vol. 1, Chaps. II and IV.
[37] E. Mathieu, "Mémoire sur le mouvement vibratoire d'une membrane de forme elliptique," J. Math. Pures Appl. **13**, 137 (1868).
[38] C. Cohen-Tannaoudji, B. Diu, and F. Laloe, *Quantum Mechanics* (Wiley, New York, 2020), Vol. 1, p. 415.